

CycleGAN integration of high-resolution crooked lines into 3D seismic volumes: Enhancing data set resolution on the Loess Plateau, China

Dawei Liu¹, Yijie He², Xiaokai Wang², Mauricio D. Sacchi³, Wenchao Chen², Fei Li⁴, Juan Chen⁴, and Yang Mu⁵

ABSTRACT

The Loess Plateau in China presents a formidable challenge for seismic exploration due to its thick, porous surface loess layers that severely attenuate high-frequency seismic waves, degrading the resolution of conventional 3D acquisition. However, the region's unique topography, crisscrossed by deep gullies formed through consistent rainfall erosion, provides a natural solution to acquire high-resolution (HR) data. With thin or absent loess cover, these gullies delineate natural pathways ideal for 2D crooked-line seismic surveys, where reduced loess interference preserves high-frequency content. Accordingly, these 2D surveys deliver better resolution than traditional 3D acquisition in the loess-covered areas. Their seismic response distributions are expected to closely resemble those of a hypothetical HR 3D data set unaffected by loess attenuation. Although these localized 2D surveys capture geologically representative HR features, existing methods struggle to extrapolate their high-frequency characteristics to broader 3D

volumes, limiting their ability to mitigate loess-induced resolution loss. To bridge this gap, we use a cycle-generative adversarial network under weak supervision to enhance 3D data resolution by leveraging unpaired 2D HR crooked-line data. Specifically, our approach transfers high-frequency features from 2D profiles to 3D volumes processed by conventional swath techniques through a bidirectional cycle structure, enforcing cross-distribution consistency while preserving geologic integrity. Custom loss functions and data augmentation further address spectral mismatches and stabilize training under loess-induced complexity. Synthetic and field experiments demonstrate that our method effectively captures HR characteristics of 2D data and recovers high-frequency content attenuated by loess in 3D data. Our approach achieves improved fidelity and noise robustness compared with traditional spectral whitening and zero-phase spiking deconvolution. This work underscores the untapped potential of integrating spatially sparse but information-rich 2D surveys with modern deep-learning methods to overcome persistent resolution limitations in seismic exploration.

INTRODUCTION

The Loess Plateau contains rich mineral resources (Yurui et al., 2021) and plays a crucial role in economic development through resource exploration. Seismic exploration is critical to understanding subsurface geologic formations and managing these resources. However, the Plateau's vast loess deposits and intricate, gully-crossed topography, as shown in Figure 1, present significant

challenges for seismic data acquisition. Specifically, the near-surface region of the Loess Plateau is characterized by a stratified structure comprising layers of loess, silt, and sandstone. The surface loess layer has a thickness ranging from 100 to 300 m and is characterized by low density, low water content, and high porosity. The porous nature of loess causes rapid seismic energy dissipation, degrading wave amplitude and frequency as it penetrates deeper. This attenuates high-frequency components significantly, which are

Manuscript received by the Editor 4 August 2024; revised manuscript received 20 February 2025; published ahead of production 12 March 2025; published online 11 June 2025.

¹Xi'an Jiaotong University, School of Information and Communications Engineering, Xi'an, China and University of Alberta, Department of Physics, Edmonton, Alberta, Canada. E-mail: 409791715@qq.com.

²Xi'an Jiaotong University, School of Information and Communications Engineering, Xi'an, China. E-mail: 13186150985@163.com; xkwang@xjtu.edu.cn; wenchchen@xjtu.edu.cn (corresponding author).

³University of Alberta, Department of Physics, Edmonton, Alberta, Canada. E-mail: msacchi@ualberta.ca.

⁴National Engineering Laboratory of Low-Permeability Oil & Gas Exploration and Development, Xi'an, China and PetroChina Changqing Oilfield Company, Exploration and Development Research Institute, Xi'an, China. E-mail: lifei@petrochina.com.cn; chenjl_cq@petrochina.com.cn.

⁵PetroChina Changqing Oilfield Company, Exploration and Development Research Institute, Xi'an, China. E-mail: muyang_cq@petrochina.com.cn.

© 2025 Society of Exploration Geophysicists. All rights reserved.

essential for detailing subtle geologic structures, reducing the resolution and signal-to-noise ratio (S/N) of traditional 3D seismic surveys. As shown in Figure 1, when positioned on these shallow, porous loess layers, receiver A encounters significant wave attenuation, compromising data resolution. Therefore, advanced seismic processing techniques are vital for precise geologic interpretations and effective resource exploration.

Several methods attempt to address the preceding challenges, such as optimizing survey geometries (Yao et al., 2004; Ye, 2011; Wang et al., 2014; Tian et al., 2021) and advancing resolution enhancement algorithms. Although effective, high-density acquisition strategies are often costly and less efficient in challenging environments, such as the Loess Plateau. Common resolution enhancement algorithms such as deconvolution (Wiggins, 1978; Taylor et al., 1979; Sacchi, 1997; Sui and Ma, 2020; Zhang et al., 2022), inverse Q filtering (Wang, 2006; Xue et al., 2019; Li et al., 2020; Ke et al., 2023), spectral whitening (Bian and Zhang, 1986; Naghadeh and Morley, 2017), and blueing (Lancaster and Whitcombe, 2000; Kazemeini et al., 2010), while prevalent in the industry, often fall short in areas with complex geologic structures or high noise levels. Q -compensated migration (Zhang et al., 2013, 2024b; Wang et al., 2022a; Xu et al., 2024) is also a practical approach to compensating for seismic energy and frequency attenuation. However, it faces challenges in accurately estimating Q values, which are crucial yet difficult to determine for practical applications. Due to severe seismic wave attenuation and complex terrain, the Loess Plateau requires advanced eco-friendly and cost-effective methods beyond conventional 3D seismic techniques to bypass or mitigate wave attenuation and improve data resolution.

Crooked-line 2D seismic reflection surveys reduce environmental impact and costs (Wu, 1996; Malehmir and Bellefleur, 2016). This approach, adapting to the terrain by following the natural contours of access routes (Nedimović and West, 2003), is successfully

applied in various regions (Schmelzbach et al., 2007; Saatçilar et al., 2014; Wadas et al., 2016; Cheraghi et al., 2020; Jodeiri Akbari Fam et al., 2021). These intentionally crooked lines provide flexible acquisition strategies that accommodate geographical constraints. Because these surveys often traverse challenging terrains, they necessitate high-density profiling, where average fold coverage typically exceeds 100 traces per gather (Nedimović and West, 2003). Recent advancements show that 2D crooked-line data can yield images of higher resolution than swath 3D methods, offering valuable insights into 3D geologic structures (Nedimović et al., 2003; Kim et al., 2014; Jodeiri Akbari Fam et al., 2023).

The distinct terrain of the Loess Plateau, marked by crisscrossed gullies, offers unique prospects for seismic surveying. As shown by the blue line in Figure 1, these deep gullies, carved by long-term water and rainfall erosion, have stripped away or significantly thinned the loess cover. Positioning seismic receivers along these pathways (e.g., receiver B in Figure 1) reduces seismic wave attenuation, allowing more efficient energy transmission. This setup is particularly conducive to 2D crooked-line seismic surveys, which navigate the natural contours of these deep gullies to avoid areas where thick loess layers heavily absorb and scatter seismic waves. As a result, these 2D surveys achieve significantly higher resolution than conventional 3D methods in the same region. Therefore, in the challenging environment of the Loess Plateau, traditional 3D seismic surveys are often complemented by these specialized 2D surveys to provide additional information. The 2D HR data collected from natural gullies on the Loess Plateau closely resemble the seismic response distributions of an ideal 3D data set undistorted by loess absorption. Inspired by compressive sensing (Baraniuk, 2007), which suggests that fewer, strategically acquired samples can reconstruct a high-quality signal, we ask: can these random, sparse, yet information-rich 2D samples be used to enhance the resolution of a 3D data set?

Significant gaps exist in effectively merging sparse 2D crooked-line surveys with 3D seismic data sets. These specialized 2D surveys offer critical, high-resolution (HR) insights into the underlying geologic structures but cover limited areas. In contrast, while swath 3D seismic techniques span a larger space with additional spatial details, they yield data of comparatively lower resolution (LR) and miss many reflectors observed in two dimensions (Cheraghi et al., 2020). Their acquisition setting and processing workflow are significantly different. Accordingly, these discrepancies pose substantial challenges to comprehensive 3D resolution enhancement. Although advanced deep-learning models show promise for resolution enhancement, they primarily depend on paired training data sets (Zhang et al., 2019, 2024a, 2024c; Chen et al., 2021; Li et al., 2021). To date, they remain poorly adapted to the unique challenges of training on disparate seismic surveys, such as 2D crooked-line and 3D swath surveys, which rarely overlap (Greer and Fomel, 2018). Innovative approaches are required to improve 3D data by learning unpaired HR 2D data to overcome these barriers.

Recent advances in weak supervision (Jiang et al., 2021; Wei et al., 2021; Yang et al., 2024) show potential for enhancing seismic resolution using unpaired training samples. Cycle-generative adversarial networks (CycleGAN), augmented with a reverse generator compared with the original GAN, adopt a Cycle-in-Cycle network architecture to facilitate translation between different data set distributions (Zhu et al., 2017). In seismic processing, most CycleGAN applications focus on either supervised learning (Kaur et al., 2020;

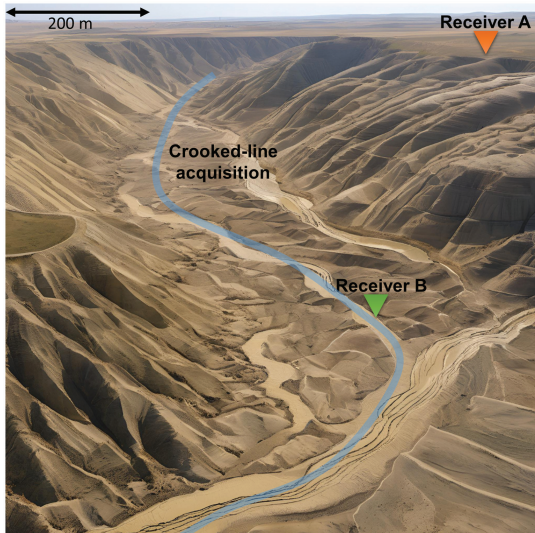


Figure 1. Illustration of seismic acquisition in a complex gully-crossed topography of the Loess Plateau. Receiver A is positioned in a typical loess-covered area where signal attenuation is pronounced. Receiver B is strategically placed along a natural gully, where the thinned loess allows for reduced attenuation and clearer signal transmission. This figure describes the feasibility of using crooked-line seismic surveys in complex terrains to enhance data resolution and accuracy.

Sun et al., 2023; Zhao et al., 2023; Goyes-Peñaflor et al., 2024; Lin et al., 2024; Xia and Dai, 2024) or semi-supervised learning (Cai et al., 2022; Wang et al., 2022b). Recently, initial studies have demonstrated the viability of weakly supervised learning with CycleGAN for improving seismic data resolution. For example, an enhanced CinCGAN architecture (Yuan et al., 2018) successfully restores high-frequency components in LR seismic data by leveraging nearby higher-resolution data sets (Liu et al., 2023). Further developments adapt this framework to 3D networks, where HR information from shallow layers is used to enhance resolution of deeper structures within the data set (Liu et al., 2025). In addition, this technique is applied to ground-penetrating radar data, with efforts to objectively assess its effectiveness against a ground-truth model (Liu et al., 2024b). These findings suggest that weakly supervised GANs effectively address data mismatch challenges in real-world applications, bypassing the need for strictly paired labels.

The HR 2D crooked-line profiles and conventional 3D data sets after resolution enhancement, both collected in the same region on the Loess Plateau, should inherently exhibit similar resolution characteristics. This distribution similarity enables weak supervision to transform characteristics between these data sets effectively. Renowned for its robust capability to translate distributions between unpaired data sets, we adapt CycleGAN to enhance the LR 3D data by learning from 2D HR data. Specifically, we develop a dual-cycle consistency approach to capture complex relationships between 2D and 3D data. This dual-cycle structure also helps address the common challenge of mismatched low-frequency components between these data sets. Our dual-cycle approach ensures more reliable and physically consistent resolution enhancement by enforcing reversibility and preserving the essential low-frequency structures in the transformations. We further use 3D generators to better capture spatial correlations inherent in 3D data sets. In addition, we incorporate custom loss functions, such as improved identity loss, which aligns the bandwidth of 2D HR and 3D LR data to minimize discrepancies in low-frequency characteristics, and data augmentation techniques to stabilize the training process. These innovations collectively address the challenge of transferring resolution features while maintaining data integrity.

The remainder of this paper is organized as follows: the “Method” section describes our weakly supervised CycleGAN framework, focusing on its dual-cycle architecture and custom loss functions. The “Examples” section presents synthetic and field experiments, along with implementation details and evaluation metrics, including a comparative analysis with traditional methods. The “Discussion” section explores key challenges in processing 2D crooked-line profiles and proposes potential future improvements.

METHOD

We begin by introducing specific mathematical notation used in this study. The tensor \mathcal{X} , represented as $\mathcal{X} \in \mathbb{R}^{i \times x \times t}$, embodies a 3D structure with inline i , crossline x , and time t dimensions. Its L_2 norm can be expressed as $\|\mathcal{X}\|_2 = \sqrt{\sum_{i,x,t} \mathcal{X}_{i,x,t}^2}$. This norm quantifies the overall magnitude of the tensor across its entire 3D space. Similarly, the matrix Y is defined as $Y \in \mathbb{R}^{n \times t}$, with dimensions of trace number n and time t .

A critical operation within our framework is the tensor inner product. The inner product between two third-order tensors, \mathcal{A} and \mathcal{B} , is denoted by $\langle \mathcal{A}, \mathcal{B} \rangle$ and calculated as follows:

$$\langle \mathcal{A}, \mathcal{B} \rangle = \sum_{i=1}^I \sum_{x=1}^X \sum_{t=1}^T \mathcal{A}_{i,x,t} \cdot \mathcal{B}_{i,x,t}, \quad (1)$$

where I , X , and T represent the total number of indices along the inline, crossline, and time dimensions, respectively. This scalar result quantifies the alignment or similarity between \mathcal{A} and \mathcal{B} by aggregating the element-wise products across all corresponding entries of the tensors, offering insights into the correlation between complex data structures.

Weak supervision with bidirectional cycle consistency

Considering the unpaired nature of 3D conventional data and 2D crooked-line seismic data, we use weak supervision to build a mapping relationship between their distributions. By referencing HR 2D data from crooked-line surveys, we aim to enhance 3D data resolution in the Loess Plateau region substantially. A straightforward approach would involve slicing the 3D data to align with the 2D crooked-line seismic data and training a network optimized for 2D inputs. After training, the network improves the resolution of entire 3D data with sequential 2D profiles, which are reassembled into the original 3D format. However, this approach has a notable limitation: the 2D network primarily processes individual 2D profiles and may not effectively capture complex 3D structural nuances, potentially leading to unstable training and compromised spatial continuity (Liu et al., 2023).

To overcome this shortcoming, we propose an innovative training workflow that maintains the dimensional integrity of the original data, thus significantly enhancing the resolution and spatial continuity of the resulting 3D seismic data. As shown in Figure 2, the proposed workflow uses CycleGAN as the backbone and adapts it to effectively transfer resolution features between 3D swath data and crooked-line 2D data. The idealized swath seismic data unaffected by attenuation and crooked-line seismic data, both from the same region on the Loess Plateau, share similar distributions of seismic responses but differ in dimensionality. Our network design accommodates dimensional differences and allows simultaneous 2D and 3D data processing. Nevertheless, their distinct acquisition designs and processing workflows complicate data correspondence. We introduce a bidirectional cycle structure in network training to reduce learning complexity. Specifically, it includes a forward cycle $\mathbb{P}_{LR} \rightarrow \mathbb{P}_{HR} \rightarrow \mathbb{P}_{LR}$ and a

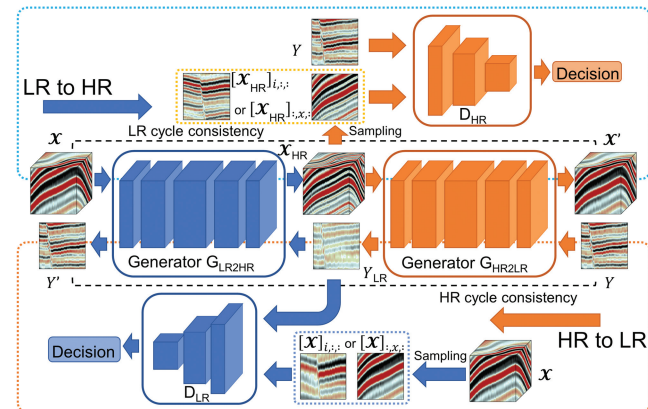


Figure 2. Workflow for the proposed weakly supervised resolution enhancement with bidirectional cycle consistency.

reverse cycle $\mathbb{P}_{\text{HR}} \rightarrow \mathbb{P}_{\text{LR}} \rightarrow \mathbb{P}_{\text{HR}}$, where \mathbb{P}_{LR} and \mathbb{P}_{HR} denote the probability distributions of LR and HR data, respectively. This dual-cycle approach stabilizes the training process and enables the network to capture more comprehensive correlations between the data sets, enhancing overall data interpretation.

The bidirectional cycle incorporates two sets of generators and discriminators. The forward generator G_{LR2HR} maps LR data from \mathbb{P}_{LR} to HR data following \mathbb{P}_{HR} , whereas the reverse generator G_{HR2LR} reverts HR data back to LR. Each cycle includes a corresponding discriminator, D_{LR} and D_{HR} , which assess the authenticity of the data according to the distributions \mathbb{P}_{LR} and \mathbb{P}_{HR} , respectively. Specifically, in the forward cycle, G_{LR2HR} learns to upgrade 3D LR seismic data to its HR counterpart. The input \mathcal{X} following P_{LR} is from 3D LR seismic data, with 2D HR seismic data $Y \sim \mathbb{P}_{\text{HR}}$ serving as learning targets. The output $\mathcal{X}_{\text{HR}} \sim \mathbb{P}_{\text{HR}}$ features enhanced resolution of the 3D LR data. In contrast, G_{HR2LR} simulates the reverse process, aiming to restore HR seismic data from P_{HR} back to its original LR distribution \mathbb{P}_{LR} . Inputting \mathcal{X}_{HR} to G_{HR2LR} yields $\mathcal{X}' \sim \mathbb{P}_{\text{LR}}$, which follows the same distribution as \mathcal{X} . The consistency of the forward cycle ensures \mathcal{X}' closely aligns with \mathcal{X} , and vice versa. The bidirectional consistency enforced through the loss function during training guarantees the reversibility of resolution enhancements, thus enhancing reliability. Notably, in the forward cycle, G_{LR2HR} and G_{HR2LR} take 3D data as inputs. In contrast, in the reverse cycle, the inputs for both generators are 2D data, which is expanded along a new axis to match the 3D convolutional kernels. This adaptation allows an integrated processing, maintaining training effectiveness across different data dimensions.

The HR discriminator D_{HR} plays a crucial role in refining the generator's performance by differentiating between generated HR data \mathcal{X}_{HR} and the real HR data Y . This differentiation guides G_{LR2HR} to produce outputs that closely follow \mathbb{P}_{HR} . Importantly, since \mathcal{X}_{HR} is 3D and Y is 2D, a random inline 2D profile $[\mathcal{X}_{\text{HR}}]_{:, :, :}$ or crossline 2D profile $[\mathcal{X}_{\text{HR}}]_{:, :, :}$ is extracted from \mathcal{X}_{HR} for discrimination with Y to ensure fairness and reduce computational costs. This selection process is integral to the adversarial framework, enhancing the realism of the generated HR data. By forcing the generated data to closely align with the target HR references, it significantly improves

the resolution enhancement ability of G_{LR2HR} . The reverse cycle mirrors this process by switching roles, where the discriminator D_{LR} evaluates the LR data, ensuring that enhancement and degradation processes maintain high fidelity relative to the corresponding data distribution. This symmetric adversarial approach in both cycles facilitates consistent, high-quality data transformations in both directions, contributing to the robustness and reliability of the model.

Network architecture design

The network architecture is shown in Figure 3, with Figure 3a illustrating the generator and Figure 3b the discriminator. The generator uses a 3D network structure to effectively capture the complex correlations inherent in 3D data while maintaining compatibility with 2D processing requirements. Data input begins at the first convolutional layer and progresses through 16 serially connected residual blocks (He et al., 2016). Each residual block, containing two convolutional layers linked by residual connections, is further enhanced by a broader cross-layer skip connection encompassing the entire group of blocks. This structure supports deeper network architectures without sacrificing training effectiveness. The extracted feature maps are then processed through several convolutional layers, culminating in an output via a Tanh activation function.

Key features of the generator are designed as follows: the absence of pooling layers preserves critical HR details vital for accurate seismic analysis, preventing the loss of valuable information. Residual blocks mitigate the vanishing gradient problem, enhancing the network's ability to learn effectively even with increased depth (He et al., 2016). Moreover, the deliberate omission of batch normalization layers increases the model's generalization ability across different seismic data sets, which is crucial for real-world applications (Wang et al., 2020). These features collectively improve the fidelity and precision of the network.

The discriminator is configured as a 2D network designed for precise discrimination. It starts with an initial convolutional layer, setting the stage for deeper feature extraction. A sequence of five convolutional blocks follows this layer to refine the feature detection process. Diverging from traditional discriminators, this model adopts

a PatchGAN architecture (Isola et al., 2017), replacing the final fully connected layer with a convolutional layer. In this way, it uncovers nuanced geophysical features by focusing on localized details. Each convolutional block comprises a convolutional layer, a batch normalization layer, and a Leaky rectified linear unit (ReLU) activation function ($\alpha = 0.2$). The Leaky ReLU function maintains gradient flow by allowing a slight, nonzero gradient when the unit is not active and thus helps maintain gradient flow. The output is then funneled through a Sigmoid activation function, resulting in a probability range from zero to one. This provides a probabilistic assessment of whether the input data conform to the desired real or fake distributions. In addition, this architecture minimizes the total number of parameters, which reduces computational load and accelerates training. The streamlined design and localized focus contribute to quicker convergence and improved discriminator efficiency, ultimately yielding higher-resolution and more precise outputs.

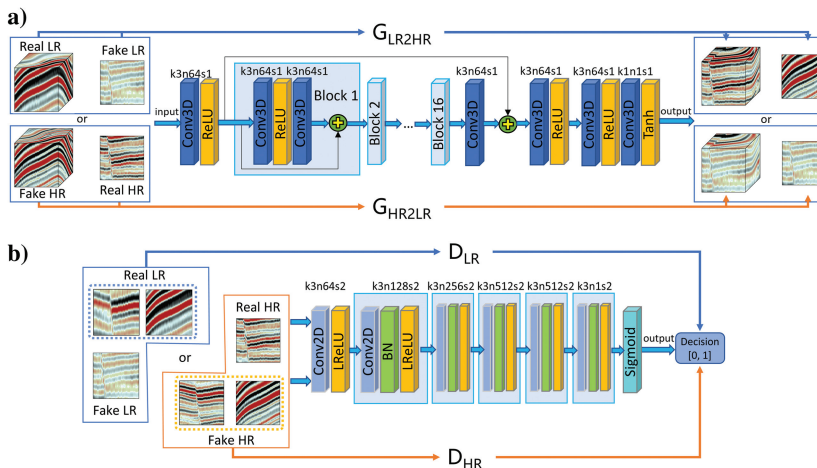


Figure 3. Network architecture. (a) The generator and (b) the discriminator. The symbol k denotes the kernel size, n specifies the number of kernels applied in each convolutional layer, and s represents the stride, which defines the step size with which the kernel moves across the input image.

Note that the generator and discriminator for both cycles share the identical architectures described previously and are trained simultaneously. However, their parameters are updated independently. On the one hand, this allows each network to adapt and optimize based on its specific role within the cycle without interference from the other's parameter adjustments, enhancing adaptability. In contrast, this streamlined training minimizes extensive hyperparameter tuning, improving training efficiency and effectiveness.

Training data set preprocessing

The original data sets are often oversized and exceed graphics processing unit (GPU) processing capabilities for network training. To address this, we partition them into fixed-size blocks with a 50% overlap, forming smaller 3D cubes and 2D patches indexed by j , designating them as \mathcal{X}_j and Y_j . We apply min-max scaling and automatic gain control (AGC) to ensure uniform signal amplitude across data sets, enhancing training efficiency.

To improve the robustness of our training data set, we implement three data augmentation strategies: inverting the amplitude, flipping spatially, and swapping spatial dimensions. These methods address imbalances in sample distribution resulting from initial uniform partitioning and increase data set diversity, which is essential for practical model training.

We manually adjust the augmentation to balance the number of samples between input data and learning targets. Ultimately, we compile M random pairs of $\{\mathcal{X}_j, Y_j\}$ for weak supervision training. This strategy ensures a comprehensive and balanced data set, creating optimal conditions for training robust neural networks capable of managing real-world data complexities.

Loss functions

In addition, the preceding training data sets, loss functions are essential as they direct network training optimization. Given the dimension mismatch between input training data and learning targets, we carefully tailor generator and discriminator loss functions for our resolution enhancement tasks.

Generator loss

We use an integrated generator loss function for updating forward and reverse generators simultaneously, customized for 2D and 3D training data. The generator loss \mathcal{L}_{Gen} comprises four parts: adversarial loss \mathcal{L}_{adv} , cycle consistency loss \mathcal{L}_{cyc} , identity loss \mathcal{L}_{idt} , and total variation loss \mathcal{L}_{TV} , defined as follows:

$$\mathcal{L}_{\text{Gen}} = w_1 \mathcal{L}_{\text{adv}} + w_2 \mathcal{L}_{\text{cyc}} + w_3 \mathcal{L}_{\text{idt}} + w_4 \mathcal{L}_{\text{TV}}, \quad (2)$$

where w_1, w_2, w_3 , and w_4 are the trade-off weights assigned to each loss. The weights should be correctly selected to ensure that these loss functions collaboratively contribute to enhancing seismic resolution. To achieve this, we empirically optimize these weights using synthetic data to find an effective combination and fine-tune them based on real data experiments.

The adversarial loss ensures that the outputs of G_{LR2HR} and G_{HR2LR} are realistic sufficient to fool D_{HR} and D_{LR} , respectively. We extract a 2D profile from the 3D data through random slicing to resolve the dimension disparity, allowing for effective integration with the 2D crooked-line data. We select the longer spatial dimen-

sion for slicing to enable a more comprehensive understanding of 3D data distribution. For instance, when the input crossline dimension exceeds its inline length, L_{adv} is defined as

$$\begin{aligned} \mathcal{L}_{\text{adv}} = & \mathbb{E}_{\mathcal{X}_j \sim \mathbb{P}_{\text{LR}}} [\log(1 - D_{\text{HR}}([G_{\text{LR2HR}}(\mathcal{X}_j)]_{i,:,:}))] \\ & + \mathbb{E}_{Y_j \sim \mathbb{P}_{\text{HR}}} [\log(1 - D_{\text{LR}}(G_{\text{HR2LR}}(Y_j)))], \end{aligned} \quad (3)$$

and vice versa. We use an alternating optimization strategy where the discriminators are fixed during generator updates to ensure a stable target and consistent gradient flow for more stable training.

Cycle consistency loss ensures outputs produced by forward and reverse generators are reversible, maintaining data consistency before and after the transformation:

$$\begin{aligned} \mathcal{L}_{\text{cyc}} = & \mathbb{E}_{\mathcal{X}_j \sim \mathbb{P}_{\text{LR}}} [\| [G_{\text{HR2LR}}(G_{\text{LR2HR}}(\mathcal{X}_j))] - \mathcal{X}_j \|_1] \\ & + \mathbb{E}_{Y_j \sim \mathbb{P}_{\text{HR}}} [\| G_{\text{LR2HR}}(G_{\text{HR2LR}}(Y_j)) - Y_j \|_1]. \end{aligned} \quad (4)$$

Identity loss, calculated using L_1 loss and multiscale structural similarity loss (Zhao et al., 2016), ensures consistency between generator input and output data:

$$\begin{aligned} \mathcal{L}_{\text{idt}} = & \mathbb{E}_{\bar{Y}_j \sim \tilde{\mathbb{P}}_{\text{LR}}} [L_1(G_{\text{LR2HR}}(\bar{Y}_j), Y_j) \\ & + L_{\text{MS-SSIM}}(G_{\text{LR2HR}}(\bar{Y}_j), Y_j)] \\ & + \mathbb{E}_{Y_j \sim \mathbb{P}_{\text{HR}}} [L_1(G_{\text{HR2LR}}(Y_j), \bar{Y}_j) \\ & + L_{\text{MS-SSIM}}(G_{\text{HR2LR}}(Y_j), \bar{Y}_j)], \end{aligned} \quad (5)$$

where $\tilde{\mathbb{P}}_{\text{LR}}$ approximates LR distribution \mathbb{P}_{LR} and we achieve this by filtering Y such that \bar{Y} matches the bandwidth of samples from \mathbb{P}_{LR} .

The total variation loss, incorporated to enhance smoothness, mitigates high gradients during training and facilitates stable convergence. For 3D data from the forward generator and 2D data from the reverse generator, it's defined as

$$\mathcal{L}_{\text{TV}} = \mathbb{E}_{Y_j \sim \mathbb{P}_{\text{HR}}} [\| \nabla_t G_{\text{HR2LR}}(Y_j) \|_1 + \| \nabla_x G_{\text{HR2LR}}(Y_j) \|_1], \quad (6)$$

where the symbols ∇_t and ∇_x represent the gradients with respect to the temporal t and spatial x dimensions, respectively.

The \mathcal{L}_{idt} and \mathcal{L}_{TV} losses are computed solely on Y . This conserves computational resources, showcasing a unique advantage of our 2D to 3D learning strategy. It also prompts generators to focus more on 2D crooked-line data, enhancing their capability to accurately represent and learn from its distribution characteristics. The subsequent experiment section validates that these 2D training losses have sufficient robustness to produce satisfactory results, consistently producing satisfactory results across various tests.

Discriminator loss

In line with the core of our bidirectional CycleGAN architecture, we use two discriminators, D_{HR} and D_{LR} , to evaluate the authenticity of outputs from the generators. These discriminators are crucial for training our model to produce high-quality seismic data following target probabilistic distributions. The discriminators' effectiveness in distinguishing between real and generated data is enhanced using a discriminator loss function structured to penalize

incorrect classifications and refine their performance over time. The formulation of this loss, based on negative log-likelihood, is as follows:

$$\begin{aligned} \mathcal{L}_{\text{Dis}} = & -\mathbb{E}_{\mathcal{X}_j \sim \mathbb{P}_{\text{LR}}} [\log D_{\text{LR}}([\mathcal{X}_j]_{i,:,:})] \\ & + \log(1 - D_{\text{HR}}(G_{\text{LR2HR}}([\mathcal{X}_j]_{i,:,:}))) \\ & - \mathbb{E}_{Y_j \sim \mathbb{P}_{\text{HR}}} [\log D_{\text{HR}}(Y_j)] \\ & + \log(1 - D_{\text{LR}}(G_{\text{HR2LR}}(Y_j))). \end{aligned} \quad (7)$$

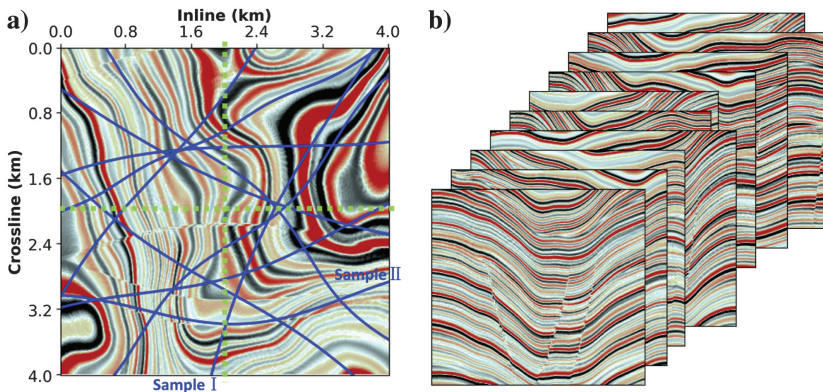


Figure 4. Simulating 2D crooked-line acquisition in a synthetic 3D seismic data set. (a) Overlaid acquisition curves. These blue curves depict potential paths for 2D crooked-line acquisition, capturing seismic data along irregular trajectories which represent natural gully terrains. The dotted green lines mark the profile locations used for subsequent evaluation. (b) Each curve leads to the segmentation of the 3D data into 2D profiles, which serve as HR targets for resolution enhancement.

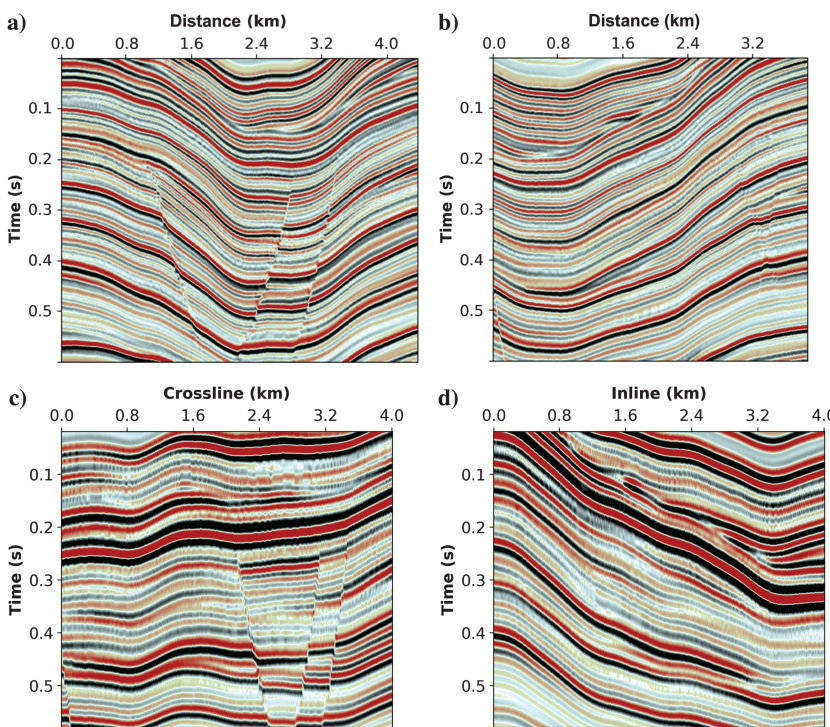


Figure 5. Examples of simulated seismic data profiles. (a) HR crooked-line data sample 1, (b) HR crooked-line data sample 2, (c) low-resolution data inline profile (inline = 200), and (d) low-resolution data crossline profile (crossline = 200).

Continuous refinement of this process strengthens the discriminators and significantly boosts generators to produce increasingly realistic seismic data, which is critical for accurate and reliable resolution enhancement.

EXAMPLES

This section evaluates our resolution enhancement method using synthetic and field data sets. The performance with synthetic data is quantitatively assessed by calculating S/N and Pearson correlation coefficients (PCC). Suppose \mathcal{X}_{HR} and \mathcal{X}_{LR} represent the synthesized HR and LR data, respectively. The enhanced resolution output from our network is represented as $\mathcal{X}_{\text{LR2HR}} = G_{\text{LR2HR}}(\mathcal{X}_{\text{LR}})$. The calculation for S/N is defined as follows:

$$\text{S/N} = 10 \log \left(\frac{\|\mathcal{X}_{\text{HR}}\|_2^2}{\|\mathcal{X}_{\text{HR}} - \mathcal{X}_{\text{LR2HR}}\|_2^2} \right), \quad (8)$$

and PCC is calculated by

$$\text{PCC} = \frac{\langle \mathcal{X}_{\text{HR}} - \mu_{\text{HR}}, \mathcal{X}_{\text{LR2HR}} - \mu_{\text{LR2HR}} \rangle}{\|\mathcal{X}_{\text{HR}} - \mu_{\text{HR}}\|_2 \cdot \|\mathcal{X}_{\text{LR2HR}} - \mu_{\text{LR2HR}}\|_2}, \quad (9)$$

where μ_{HR} and μ_{LR2HR} are the mean values of the respective tensors. These metrics are crucial indicators of the effectiveness of our method, reflecting significant resolution improvements after network processing.

Synthetic data example

Training data set construction

This section uses the open-source Synthoeseis model (Merrifield et al., 2022) to construct synthetic seismic data sets for validating our methodology. We choose this package for its capability to generate relatively large 3D models. By manually setting parameters, we derive reflection coefficients, which are then convolved with Ricker wavelets at various central frequencies to produce LR and HR 3D seismic data sets. Specifically, the 45 Hz Ricker wavelet convolution represents the HR data, and the 30 Hz wavelet represents the LR data.

The dimensions of the simulated seismic data are $400 \times 400 \times 600$ (inline, crossline, and time dimensions, respectively), with inline and crossline intervals of 10 m and a time sampling of 1 ms. To mimic natural deep gullies for 2D crooked-line acquisition, we randomly draw several sinusoidal curves across the 3D data, as shown in Figure 4a. Following these blue curves, the data are segmented into several sinusoidal cylindrical profiles with faults, as shown in Figure 4b. These profiles are used as HR targets for our CycleGAN, and the entire LR 3D data set serves as input for

the network, as exemplified in Figure 5. In addition, we compute the normalized multitrace amplitude spectra for both data sets, highlighting significant differences in spectral widths as shown in Figure 6.

Before network training, these data sets undergo AGC and normalization, as outlined in the previous section, to ensure training stability. The LR seismic data are divided into blocks of $11 \times 80 \times 80$ (or $80 \times 11 \times 80$), sampled uniformly throughout the data set. Because we are not using supervised learning, the placement of these LR cubes is not constrained by proximity to 2D curved paths, demonstrating significant acquisition flexibility. Similarly, the 3D HR data set is segmented into 80×80 sections. After data augmentation, these segments are fed into the network for weakly supervised learning. This process enables the network to learn from the distribution of randomly extracted 2D HR data, effectively enhancing the resolution of 3D LR data and facilitating unpaired resolution enhancement.

Training parameter setting

The Adam optimizer (Kingma and Ba, 2014) is used for model training, with parameters set as $\beta_1 = 0.5$, $\beta_2 = 0.999$, and $\epsilon = 10^{-8}$. Here, β_1 and β_2 control the exponential decay rates of the moving averages for the first and second moments of the gradients, respectively, influencing the speed and stability of model updates. The symbol ϵ is a small constant added to the denominator to prevent zero division during computation, ensuring numerical stability. Training samples are randomly cropped from rectangular regions of synthetic seismic profiles using uniform distribution sampling. The parameter settings in equation 2 are $w_1 = 0.05$, $w_2 = 25$, $w_3 = 5$, and $w_4 = 2$. The network starts with a learning rate of 0.0001, decaying to half every 10,000 pairs of samples over 20,000 epochs with a batch size of two. We use four NVIDIA 3090 GPUs to train the network for 2.5 h. Figure 7 shows the generator and discriminator loss curves during training. The generator loss decreases steadily, indicating consistent refinement of generated outputs. The discriminator loss exhibits minor, bounded fluctuations, which are characteristic of adversarial dynamics. These instabilities arise from the competitive interplay between the networks but eventually stabilize into equilibrium, ensuring balanced

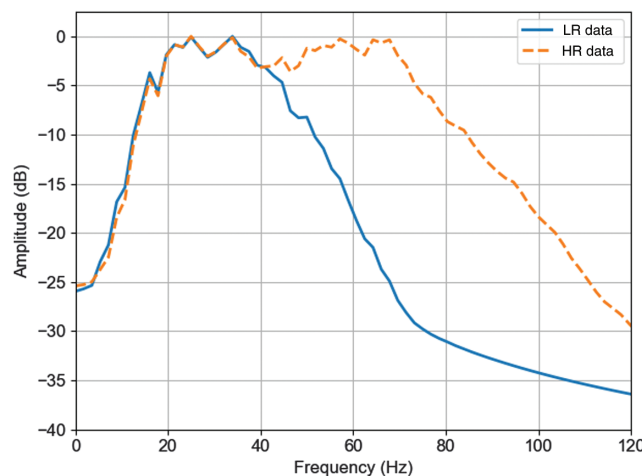


Figure 6. Comparison of normalized multitrace amplitude spectra for HR and low-resolution (LR) data.

optimization. The following results demonstrate that these fluctuations do not compromise output quality.

Results

To evaluate the effectiveness of the proposed method, we use spectral whitening (Bian and Zhang, 1986) and zero-phase spiking deconvolution (Leinbach, 1995; Robinson and Treitel, 2000) for comparison, which are widely recognized in the industry. The assessment is conducted from five perspectives: inline and crossline profiles, time slices, fault preservation, and normalized multitrace amplitude spectra. In addition, we validate the efficacy of each model component through ablation studies.

Figure 8 shows the selected inline profile (inline = 200) for validation. Figure 8a and 8b shows the LR and the corresponding HR simulated data, respectively. For comparison, Figure 8c and 8d shows the outcomes of spectral whitening and spiking deconvolution, respectively, whereas Figure 8e shows the results after resolution enhancement using the proposed network method. A comprehensive comparison of these approaches reveals that all three methods significantly improve the resolution of the LR data and effectively preserve crucial structural information, such as faults. However, the network method yields results that are more closely aligned with the HR data, demonstrating better resolution enhancement accuracy. A closer

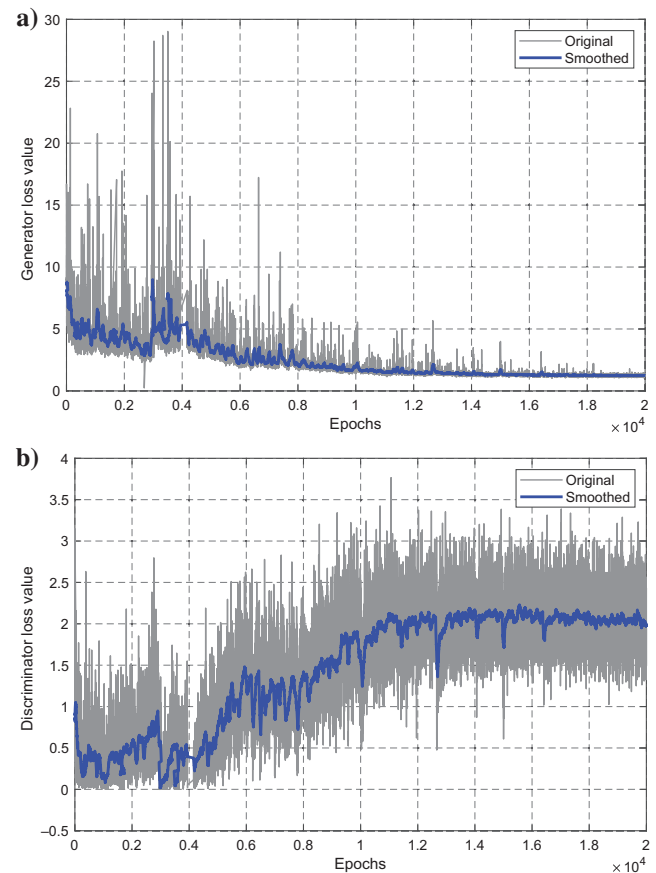


Figure 7. Training loss curves with synthetic data. (a) Generator loss and (b) discriminator loss. Both smoothed curves demonstrate stability, reflecting balanced adversarial learning and effective convergence during training.

examination of the areas highlighted in green boxes reveals that spectral whitening and spiking deconvolution result in blurred seismic events and poorly resolved underlying structures. In contrast, the network method successfully recovers fine geophysical details, providing a more accurate representation of geologic sequences. Furthermore, the yellow arrow highlights regions where the network method maintains better event continuity. In contrast, spectral whitening and spiking deconvolution fail to preserve local continuity despite their overall effectiveness. This comparative analysis underscores the advantage of the proposed method in enhancing seismic resolution compared with traditional methods.

Figure 9 shows the results from a crossline profile (crossline = 200), offering a direct comparison between the spectral whitening shown in Figure 9c, spiking deconvolution presented in Figure 9d, and our network method shown in Figure 9e. The network method significantly enhances LR data's resolution while preserving the original stratigraphic details. This precision identifies subtle geologic variations indistinguishable from LR data. In addition, the outputs from our method closely match the corresponding HR data shown in Figure 9b, illustrating its accuracy in improving seismic resolution. The green-boxed areas, characterized by parallel layers, serve as ideal regions for validating fidelity after resolution enhancements. Spectral whitening produces discontinuous seismic events that complicate strata sequence interpretation, while spiking deconvolution introduces artifacts that distort seismic events. These artifacts potentially lead to misinterpretation of geologic structures and sequences. In contrast,

the network method provides a distinct and coherent delineation of seismic layers, facilitating more reliable geologic analysis. Moreover, as indicated by red arrows, both conventional methods exhibit notable limitations: spectral whitening shows boundary distortions at window function boundaries for certain structures, and spiking deconvolution fails to achieve high-fidelity resolution enhancement. In contrast, our proposed method preserves global structural integrity, demonstrating its enhanced capability in enhancing seismic resolution.

Figure 10 shows the results at a 300 ms time slice, comparing three techniques. Although all methods enhance clarity and preserve fault structures, they render geologic details differently. Spectral whitening, as shown in Figure 10c, increases the visibility of seismic layers but often produces less distinct interfaces, leading to blurred depictions of structural complexities. Spiking deconvolution, shown in Figure 10d, performs slightly worse than spectral whitening, as it fails to enhance layer clarity adequately. This shortcoming limits its ability to resolve intricate details, particularly within the green-boxed regions, which are critical for accurate geologic interpretations. In contrast, our network method, shown in Figure 10e, delivers sharper interfaces and more defined geologic features, particularly around crucial boundaries. This precision is essential for accurate subsurface mapping and resource identification. Within the green-boxed areas, the network method significantly outperforms the other two methods by effectively reconstructing subtle details and preserving layer continuity, whereas conventional methods demand careful trade-offs.

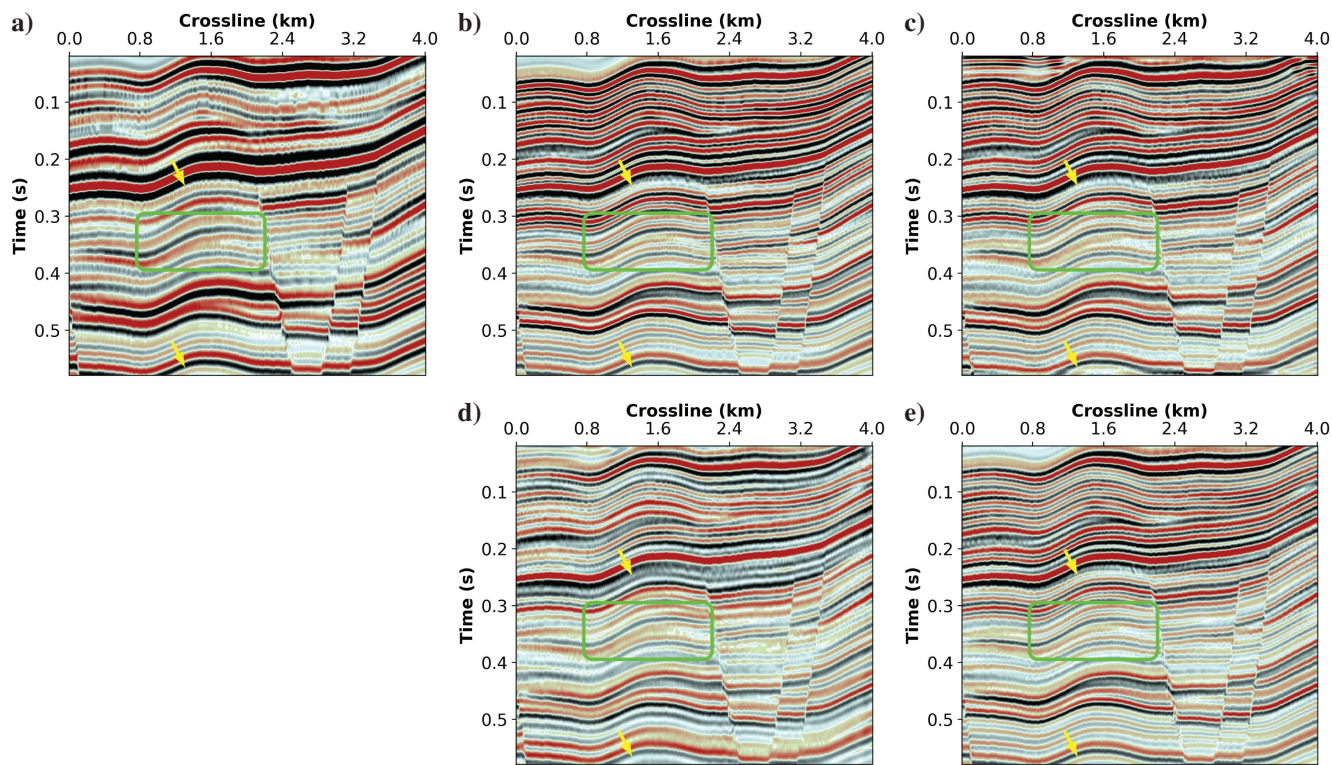


Figure 8. Comparison of inline profile results (inline = 200) of synthetic data. (a) Original LR data, (b) corresponding HR data, (c) results by spectral whitening, (d) results by zero-phase spiking deconvolution, and (e) results by the proposed method. The green boxes highlight areas where the proposed method distinctly improves clarity and reveals fine geologic structures, in contrast to the blurred results from spectral whitening and spiking deconvolution. The yellow arrows point to regions where our method demonstrates superior continuity of seismic events.

In addition, red arrows highlight complex formations indistinct in the original LR data. Although spectral whitening and spiking deconvolution obscure these critical details, our network method restores them effectively.

We calculate the positive curvature attribute (Chopra and Marfurt, 2007; Wang et al., 2018) for this time slice to further assess the preservation of fault structures. As shown in the red circle regions of Figure 11, our network provides clear and continuous curvature attributes, enhancing fault clarity and continuity. This contrasts with the conventional methods, which often yield fragmented or less coherent curvature attributes, hindering fault interpretation. These results confirm the network method's satisfactory ability to manage complex geologic formations, proving it a valuable tool for enhancing seismic data resolution and ensuring reliable subsurface interpretations.

Preserving low-frequency information while expanding effective bandwidth to enhance high-frequency characteristics is crucial for improving seismic resolution. As shown in Figure 12, the normalized multitrace amplitude spectra provide key insights. All three methods effectively enhance high-frequency features by significantly extending bandwidth, which is essential for detailed geologic examination. However, they exhibit varying performance in balancing bandwidth extension with spectral fidelity. Spectral whitening achieves the highest bandwidth extension but it inevitably introduces high-frequency artifacts that mismatch the HR data beyond 100 Hz (~20 dB). These artifacts reflect the inherent trade-off in spectral whitening between aggressive bandwidth extension and maintaining spectral fidelity,

which can limit its effectiveness for geologic applications that require precise high-frequency details. Spiking deconvolution also extends the low-frequency range, which could be a potential advantage. However, since we are working with land data that typically contain ground roll and scattered noise, the reliability of this low-frequency extension is questionable, as it may amplify unwanted noise. In addition, spiking deconvolution exhibits limited resolution enhancement overall due to the sharp drop-off in its amplitude spectrum approximately 70 Hz. In contrast, our network method strikes the best balance among the three techniques. It faithfully retains low-frequency features below 20 Hz, closely aligning with the original LR data while extending bandwidth to higher frequencies. Beyond 100 Hz, the network provides a natural and accurate high-frequency response, avoiding the artifacts seen in spectral whitening and more closely matching the HR data. By combining effective bandwidth extension with detail preservation, this balanced performance renders the network method particularly valuable for detailed geologic analysis.

Ablation study

We conduct ablation experiments to assess the impact of the proposed training strategies. These experiments involve removing various loss functions and data augmentation strategies during the training process while keeping the same network architecture or training parameters. We calculate S/N and PCC between each network output and HR data to measure their effectiveness. For comparative analysis, spectral whitening results are also evaluated.

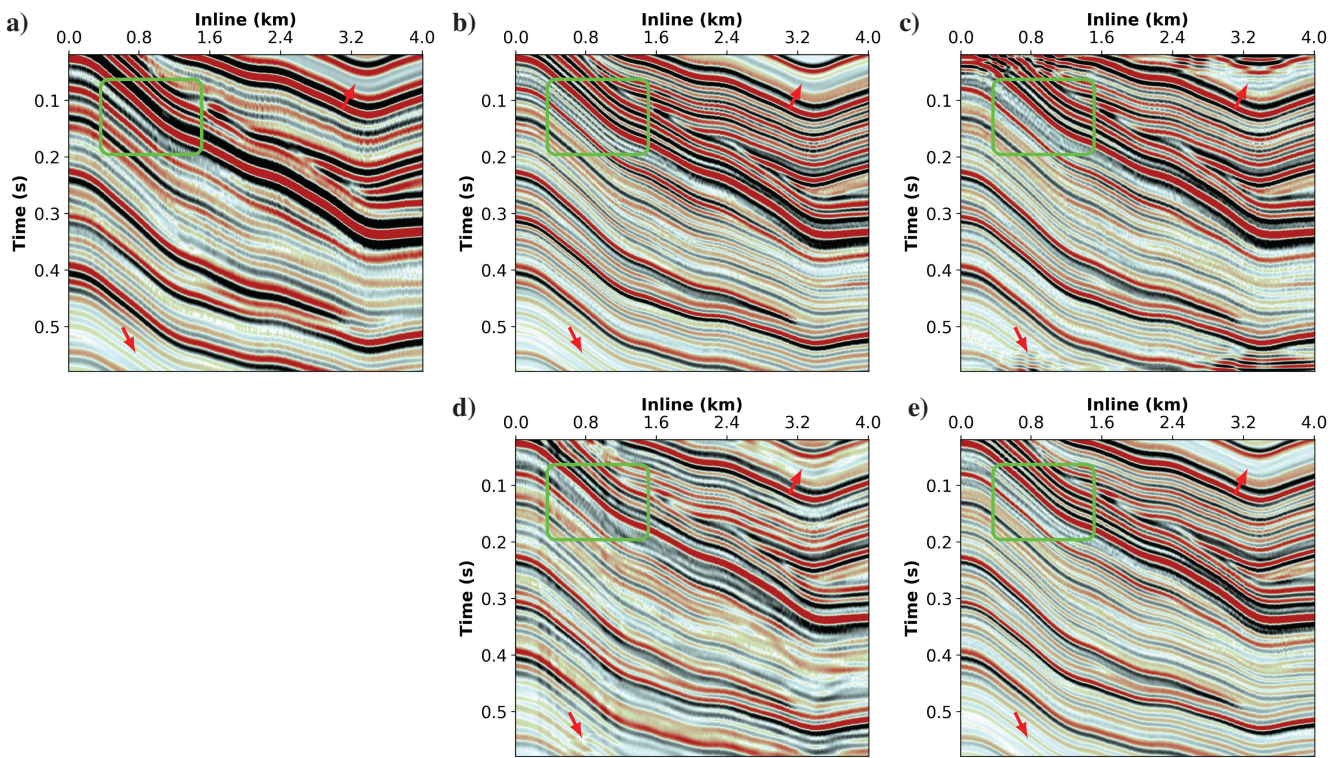


Figure 9. Comparison of crossline profile results (crossline = 200) of synthetic seismic data. (a) Original LR data, (b) corresponding HR data, (c) results by spectral whitening, (d) results by zero-phase spiking deconvolution, and (e) results by the proposed method. The green boxes illustrate clear strata layers, validating our method's effectiveness and fidelity. The red arrows mark structural distortions introduced by spectral whitening and artifacts from spiking deconvolution, underscoring our method's superiority in maintaining geologic integrity.

The results, as shown in Table 1, demonstrate the significant impact of the adversarial loss \mathcal{L}_{adv} on network training, illustrating the generator's robust capability to capture HR data features under diverse input and label data dimensions. Data augmentation plays a less prominent role, highlighting the necessity for augmentation since 3D networks require larger data sets. The cycle consistency loss \mathcal{L}_{cyc} also proves crucial, emphasizing the importance of imposing consistency constraints on the generator. Other loss functions are less essential but also contribute to the resolution improvement process, with their removal leading to decreased PCC and S/N. Compared with spectral whitening and zero-phase spiking deconvolution, the network approach produces results that more closely align with HR data, highlighting its effectiveness in enhancing seismic data resolution and enabling more precise geologic analysis.

We further evaluate the influence of the training number of crooked lines. As shown in the lower portion of Table 1, increasing the number of crooked lines leads to notable performance improvements. This underscores the value of diverse training data, as crooked lines introduce realistic sampling irregularities that enhance the network's ability to generalize to complex 3D patterns. Since performance gains taper off beyond six crooked lines, we set the number to ten in our complete framework to approach full performance. Remarkably, even training with a single crooked line achieves results comparable to traditional methods. This demonstrates that even limited HR 2D

data can enable the network to capture representative geologic features and recover fine-scale details, effectively bridging the resolution gap between sparse 2D surveys and large-scale 3D data sets.

Real data example

Training data set construction

We use a 3D poststack data set obtained via a swath acquisition from the Loess Plateau and its complementary 2D HR crooked-line data from the same work area to verify our method. Figure 13 shows the base map of the surveyed area, showing the trajectories of six crooked-line seismic surveys (R1–R6) mapped on the 3D inline-crossline grids from the swath acquisition. These surveys follow naturally formed gullies with thin loess layers, which enable HR 2D seismic profiling by minimizing loess attenuation. Their trace lengths are 2645, 2049, 1317, 1472, 3509, and 2632, with a time sampling of 2 ms. A time window of 0.5 to 2.0 s is selected for network training. Two examples of these 2D HR crooked lines are shown in Figure 14a and 14b, providing a more precise depiction of geologic sequences.

The 3D LR data set has a size of 1164×2400 (inline \times crossline) and shares a time sampling of 2 ms with 2D data. Inline and crossline intervals are 20 m. Because its boundary has low fold coverage, we select a high S/N block near the center with dimensions

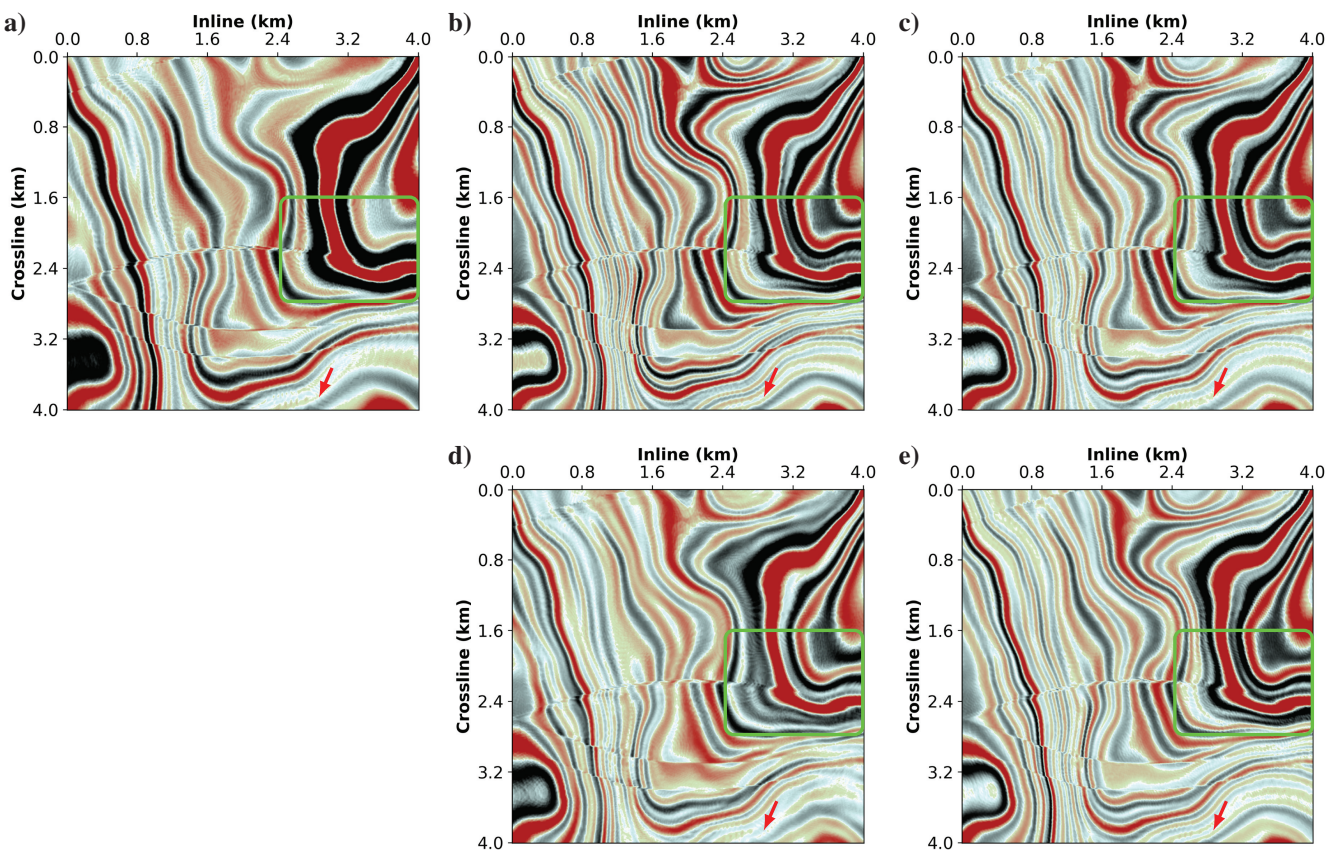


Figure 10. Comparison of time-slice results (time = 300 ms) of synthetic seismic data. (a) Original LR data, (b) corresponding HR data, (c) results by spectral whitening, (d) results by zero-phase spiking deconvolution, and (e) results by the proposed method. The green boxes delineate areas where the network method exhibits better clarity over spectral whitening and spiking deconvolution in capturing intricate geologic details. The red arrows point to previously unclear complex formations in the LR data, which are now clearly restored by the network method.

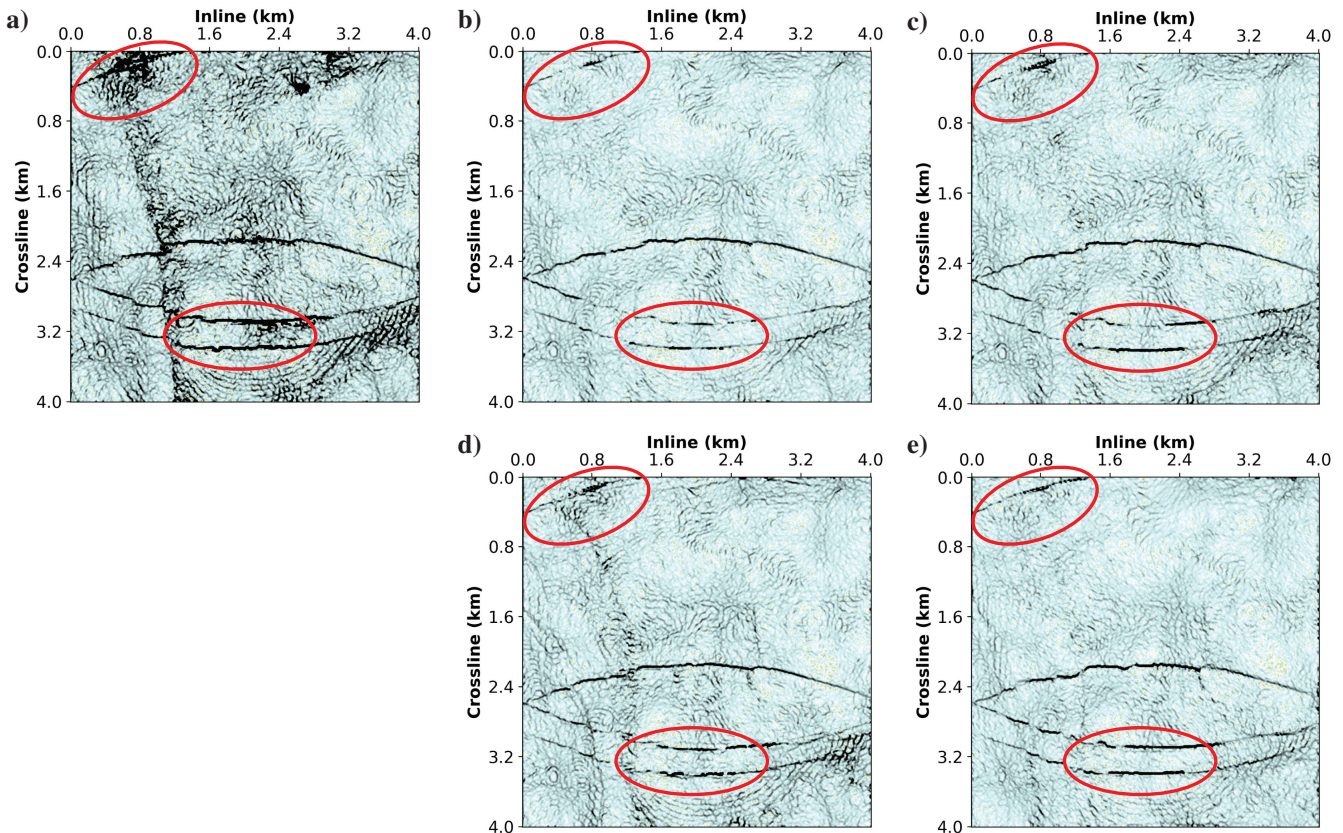


Figure 11. Comparison of positive curvature attribute for a time slice (time = 300 ms) of synthetic seismic data. (a) Original LR data, (b) corresponding HR data, (c) results by spectral whitening, (d) results by zero-phase spiking deconvolution, and (e) results by the proposed method. The boxes highlight areas where the network method provides better clarity and continuity in capturing fault structures compared with spectral whitening and spiking deconvolution.

800 × 2000 to enhance our training. The analysis time window still ranges from 0.5 to 2.0 s to ensure consistency. Posttraining, we conduct comprehensive testing on the entire data set. Figure 14c and 14d shows LR inline and crossline profiles from the 3D data set.

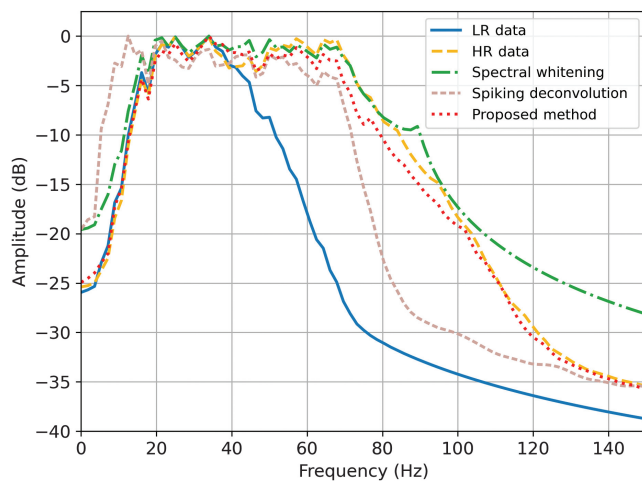


Figure 12. Comparison of normalized multitrace average amplitude spectra of synthetic seismic data.

Table 1. Quantitative comparison of synthetic results across different methods and variants.

Category	Methods	PCC	S/N
Comparative methods	Spectral whitening	0.9253	8.420
	Zero-phase spiking deconvolution	0.8936	6.7147
	Proposed framework (complete)	0.9610	11.169
Ablations	Without \mathcal{L}_{adv}	0.8478	4.762
	Without \mathcal{L}_{cyc}	0.8682	6.050
	Without \mathcal{L}_{TV}	0.9495	9.956
	Without \mathcal{L}_{adv}	0.9441	9.629
	Without data augmentation	0.8365	4.707
	With 1 crooked line	0.9045	8.194
	With 2 crooked lines	0.9358	8.971
	With 4 crooked lines	0.9405	9.379
	With 6 crooked lines	0.9524	10.542
	With 8 crooked lines	0.9572	10.980

Bold values indicate the best performance (highest SNR and PCC).

These profiles exhibit similar geologic structure features to HR data in Figure 14 but at LR. A normalized multichannel amplitude spectrum is shown in Figure 15, highlighting significant spectral differences. These two data sets provide precise support for validating our resolution enhancement methods.

Training parameter setting

We also use the Adam optimizer to train the CycleGAN network for real data, configured with the following parameters: $\beta_1 = 0.5$,

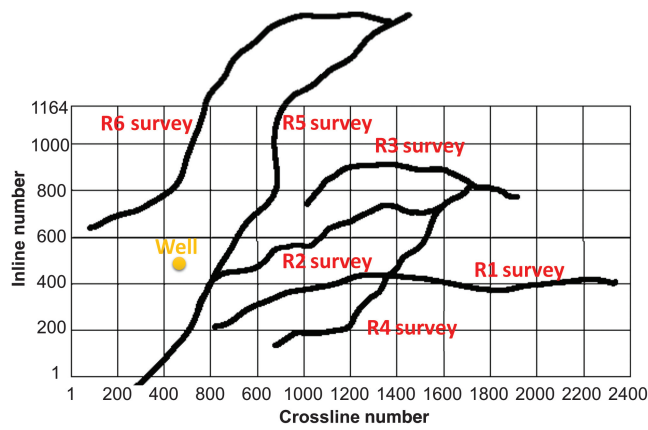


Figure 13. Base map of the real data survey. Crooked-line seismic surveys (R1–R6) mapped on the 3D inline-crossline grids from the swath acquisition, performed along naturally formed gullies that enable HR 2D seismic profiling by minimizing loess attenuation.

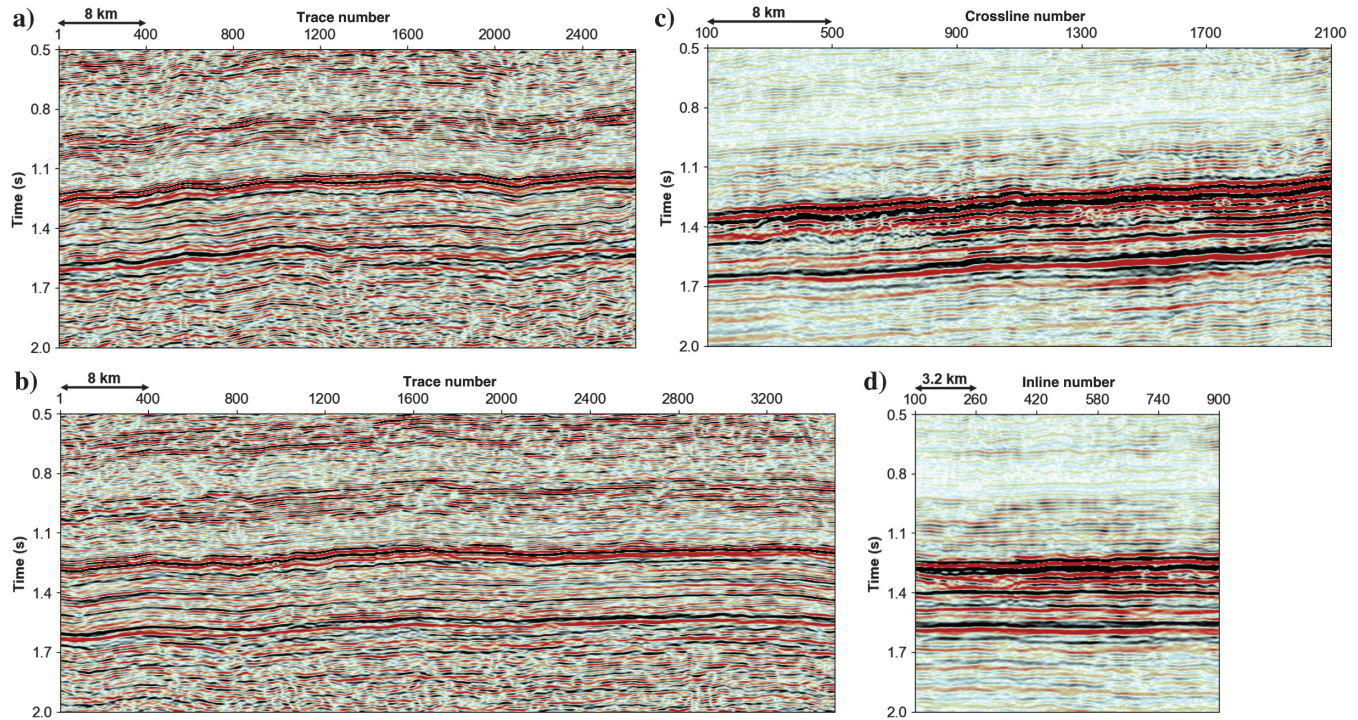


Figure 14. Seismic profiles comparison. (a) HR crooked-line data from the R1 survey, (b) HR crooked-line data from the R5 survey, (c) inline profile from LR 3D data, and (d) crossline profile from LR 3D data. This figure juxtaposes various seismic profiles, illustrating differences in resolution and similarities in stratigraphic structures across multiple surveys.

$\beta_2 = 0.999$, and $\epsilon = 10^{-8}$. Training samples are randomly cropped from selected regions of 3D data and 2D profiles using a uniform distribution. For the parameters outlined in equation 2, the settings are maintained to $w_1 = 0.05$, $w_2 = 25$, $w_3 = 5$, and $w_4 = 2$. The network commences with an initial learning rate of 0.0001, halved every 10,000 sample pairs over 20,000 epochs. The batch size for input data is still two. This constant parameter setting confirms the robustness of our method, which is crucial for ensuring its wide applicability without extensive parameter tuning.

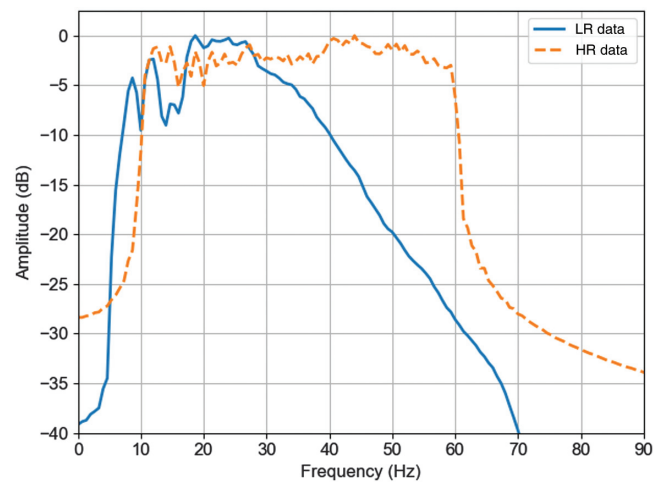


Figure 15. Comparison of normalized multichannel amplitude spectrum for real data.

Results

Our method is applied to the complete 3D LR data, showcasing enhanced results for Figure 14c and 14d. As shown in Figure 16, the spectral whitening and our method significantly improve the resolution for the inline = 700 and crossline = 1300 profiles. These

profiles exhibit substantial resolution improvements while maintaining energy consistency observed in the original LR data. This consistency across different profile orientations confirms the reliability and effectiveness of our method, demonstrating its capability to deliver enhanced seismic interpretations by capturing intrinsic property distributions within seismic data.

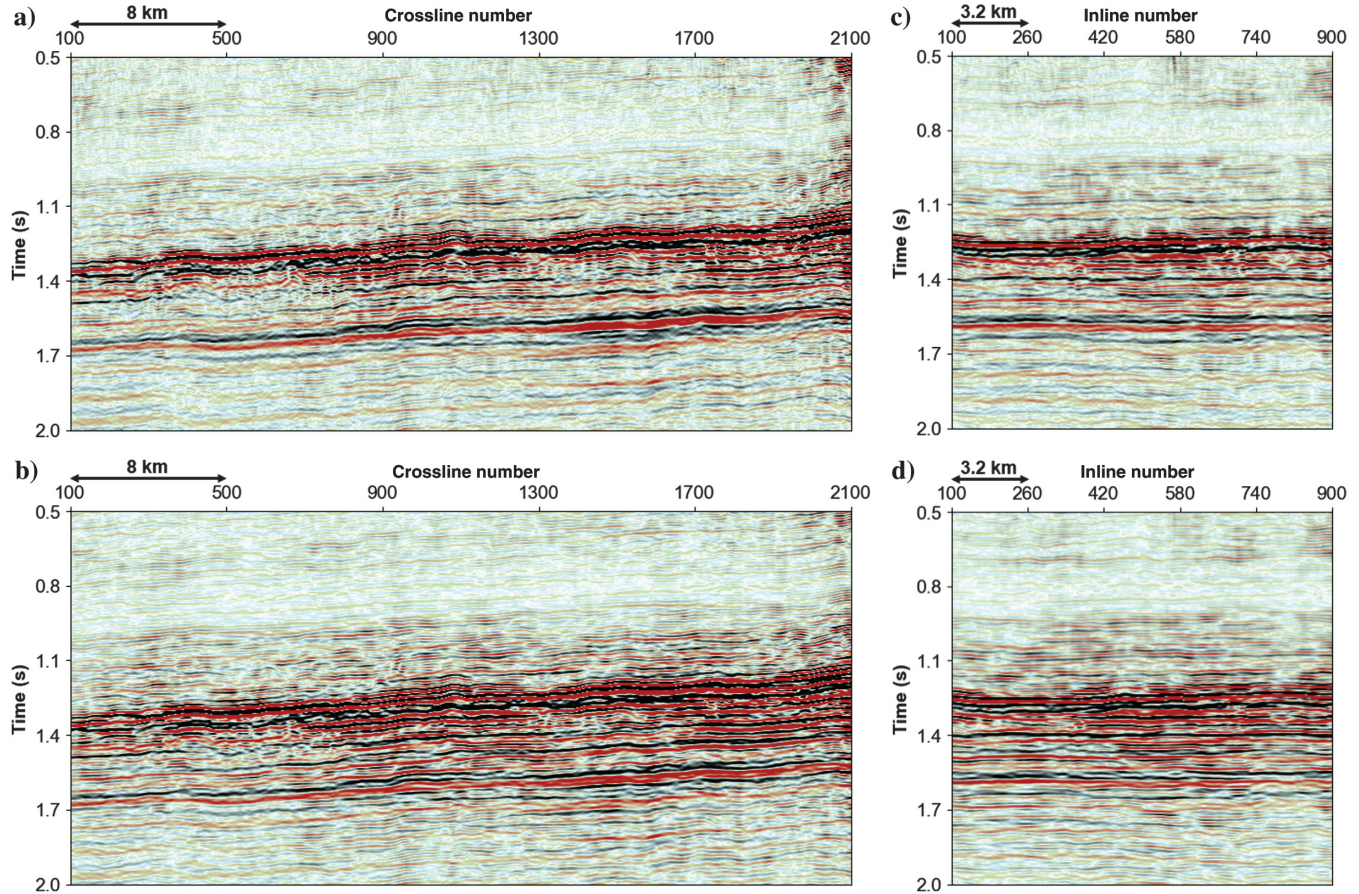


Figure 16. Enhanced resolution for seismic profiles of Figure 14c and 14d. (a) Improved inline profile at inline = 700 by spectral whitening, (b) improved inline profile at inline = 700 by the proposed method, (c) improved crossline profile at crossline = 1300 by spectral whitening, (d) improved crossline profile at crossline = 1300 by the proposed method.

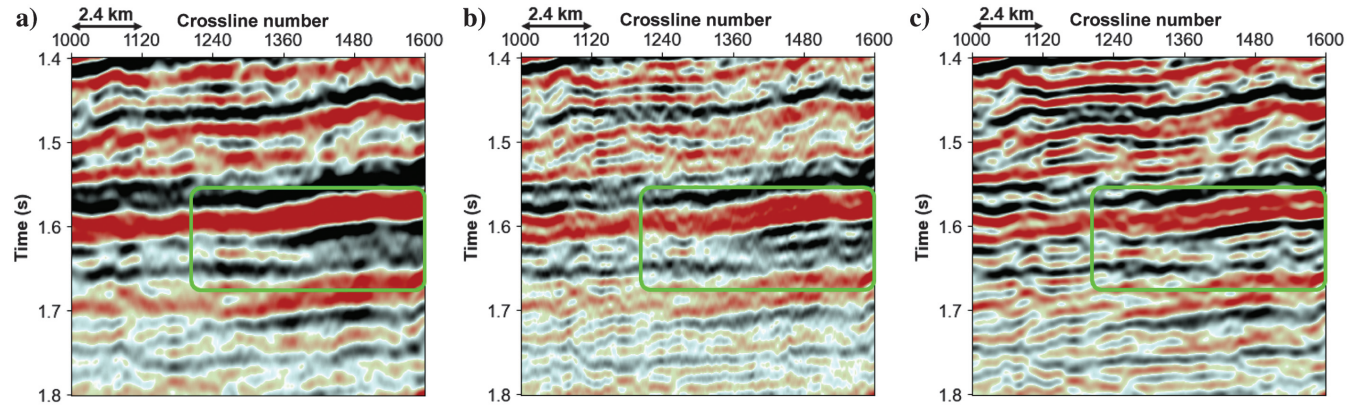


Figure 17. Magnified comparative analysis of inline = 700 profile. (a) Original LR data, (b) results by spectral whitening, and (c) results by the proposed method. Our method significantly improves reflection continuity within the marked green box areas, revealing subtle geologic features.

We also illustrate magnified results for detailed comparison. Figure 17 shows enlarged images from inline = 700. The magnified view in Figure 17a shows the original LR data, whereas Figure 17b shows the spectral whitening results, which produce sharper layers with finer stratigraphic details. The magnified view in Figure 17c shows our results. The network output shares strong structural similarity with spectral whitening, demonstrating remarkable clarity in geologic features. However, our method yields reflections with increased continuity and a significant reduction in noise levels, allowing for clearer identification of geophysical boundaries. Specifically, our method amplifies weak seismic signals within the marked green box, unveiling previously obscured geologic features. This improvement is crucial for comprehensive subsurface mapping and reduces seismic interpretation uncertainties. In contrast, while spectral whitening clarifies some details, it also produces blurred reflections that may introduce uncertainties.

Similar observations are evident from the magnified crossline profile at crossline = 1300 in Figure 18. Both methods enhance the resolution of geologic formations beyond the original profile. However, as highlighted by the green boxes, our method delineates geologic interfaces more distinctly, where spectral whitening introduces abrupt discontinuities that complicate geologic analysis. These comparisons underscore our method's effectiveness in enhancing seismic resolution compared with traditional approaches, making it a more reliable tool for seismic exploration.

Figures 19 and 20 further show results for time slices at time = 1420 ms and time = 1600 ms, respectively. Both enhancement methods provide a clearer visualization of subtle changes, allowing the identification of minor depositional features. The results remain consistent with the overall structures obtained from spectral whitening, confirming the reliability of our method. However, there are notable differences in the details between these two methods.

In the green-boxed area shown in Figure 19, our method maintains a high S/N. It sharply delineates the boundaries between geologic features, facilitating a deeper understanding of the sedimentary environment. In contrast, these distinctions are not sufficiently pronounced by spectral whitening. Moving to Figure 20, the effectiveness of our method becomes even more evident as it goes deeper. As the green boxes indicate, our method detects subtle changes in facies that are less discernible in the original time slices. The enhanced time slices provide more precise visualizations and identifications of critical

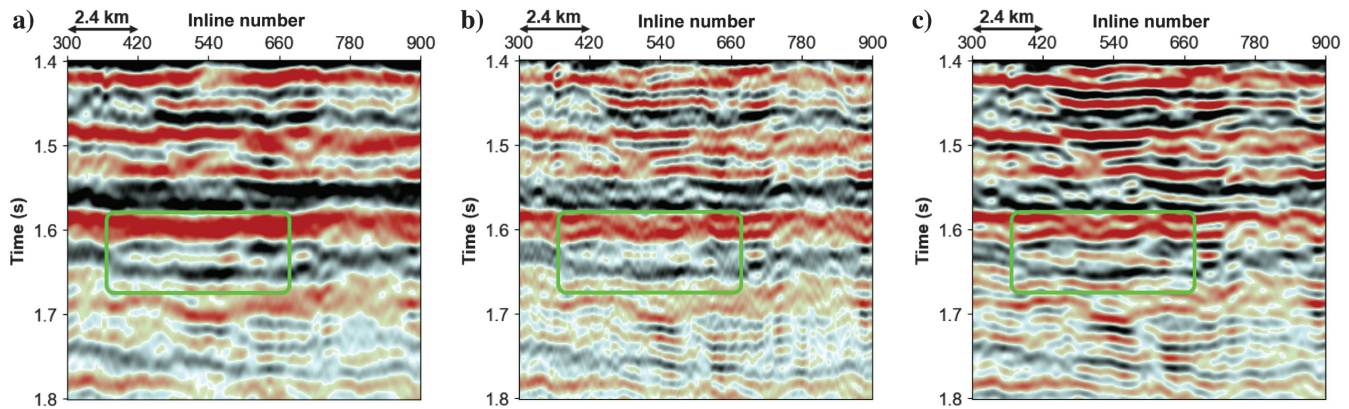


Figure 18. Magnified comparative analysis of crossline = 1300 profile. (a) Original LR data, (b) results by spectral whitening, and (c) results by the proposed method. As indicated in the green box regions, our approach provides a more precise delineation of geologic boundaries than spectral whitening, which introduces discontinuities.

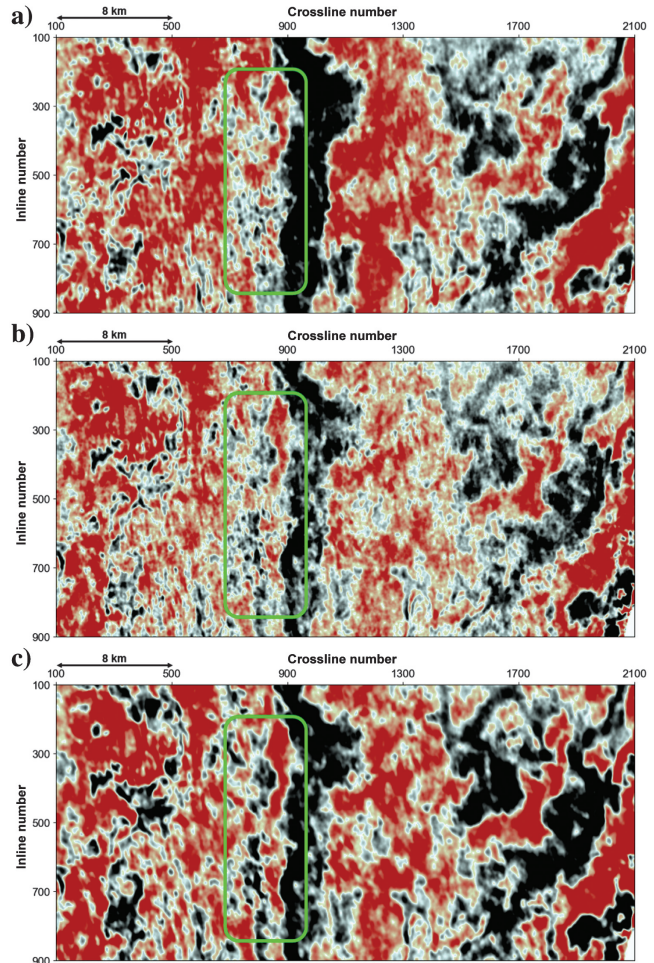


Figure 19. Enhanced resolution results at time slice of time = 1420 ms. (a) Original LR data, (b) results by spectral whitening, and (c) results by the proposed method. The green box highlights that our method more effectively characterizes sedimentary boundaries with a higher S/N than spectral whitening.

depositional features, which is crucial for a comprehensive understanding of reservoir heterogeneity. This refined detection capability ensures a more accurate and detailed representation of the subsurface, affirming our methodology as a valuable tool for advanced geophysical analysis and effective reservoir characterization.

Figure 21 shows a comparative multitrace amplitude spectrum analysis. Spectral whitening and network methods significantly enhance the high-frequency components of the original LR data. They extend the effective bandwidth similarly while preserving the low-frequency components. However, the network aligns more closely with the original data than spectral whitening at the lower frequencies. Particularly approximately 15 Hz, our results follow the original amplitude decrease, capturing more detailed information without compromising signal quality. In contrast, spectral whitening smooths the spectrum, potentially distorting key low-frequency components.

We perform a well-log tie analysis to assess our approach's effectiveness. For this analysis, statistical wavelets are extracted from nine neighboring traces within a time window of 1.0 to 1.4 s,

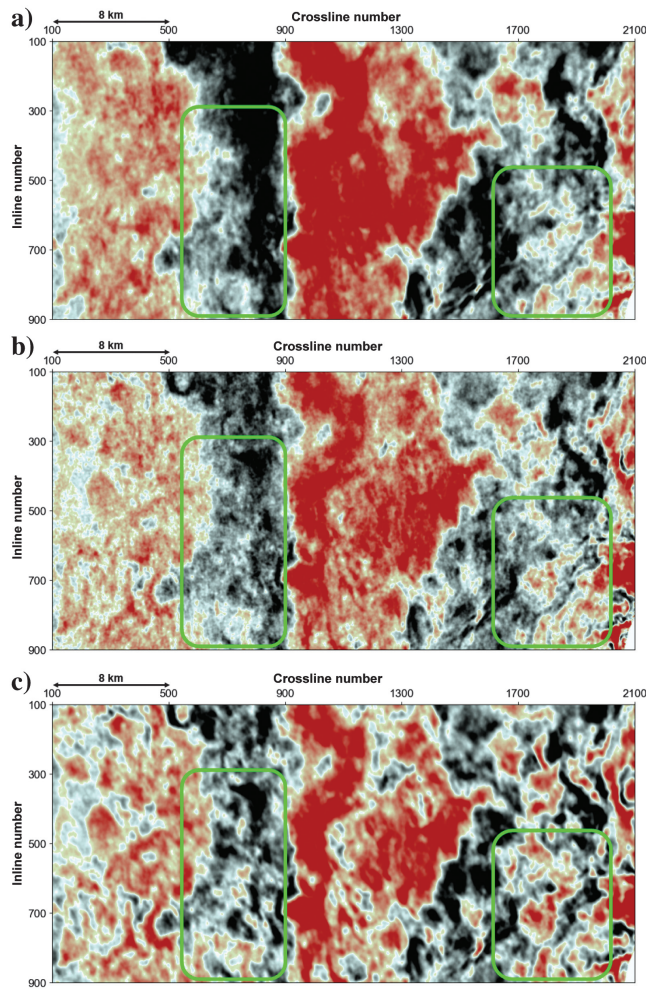


Figure 20. Enhanced resolution results at time slice of time = 1600 ms. (a) Original LR data, (b) results by spectral whitening, and (c) results by the proposed method. The green boxes underscore our advanced capabilities for identifying minor depositional features, showcasing enhanced detail and accuracy.

capturing the target layer of interest. In Figure 22a, the original seismic data exhibit strong alignment with the synthetic data, achieving a cross-correlation coefficient of 0.822, which confirms a reliable tie to the well log. Although spectral whitening (Figure 22b) enhances visual resolution, it yields a lower crosscorrelation of 0.689, indicating moderate accuracy and some misalignment with the well-log data. In contrast, our proposed method (Figure 22c) achieves a crosscorrelation of 0.766, demonstrating improved alignment with the well-log data compared with spectral whitening. A visual comparison further reveals that our approach resolves subtle layers that are less clearly defined in LR data, offering a more detailed representation of complex geologic structures. These quantitative findings, along with the observed qualitative improvements, establish our method as a valuable tool for seismic resolution in this challenging loess region.

DISCUSSION

Addressing challenges in crooked-line processing for reliable HR feature extraction

The resolution enhancement achieved by our method relies heavily on the HR features extracted from 2D crooked-line data. Inappropriate processing of crooked-line data risks introducing amplitude and phase distortions, which can manifest as acquisition footprints or false stratigraphic features. These artifacts may mislead the network into amplifying errors rather than enhancing resolution. Therefore, careful processing of 2D crooked-line surveys is critical to ensure accurate subsurface representation and reliable feature extraction.

Midpoint dispersion

The nonlinear and irregular geometry of crooked-line surveys leads to unevenly distributed midpoints, causing them to deviate from the ideal linear geometry and disperse laterally (Nedimović et al., 2003; Schmelzbach et al., 2007). This irregularity results in spatial sampling inconsistencies, which can smear geologic structures, particularly in complex subsurface regions. To mitigate these effects, trace regularization using a nonuniform Fourier transform (Duijndam et al., 1999; Keiner et al., 2009) or other latest interpolation techniques

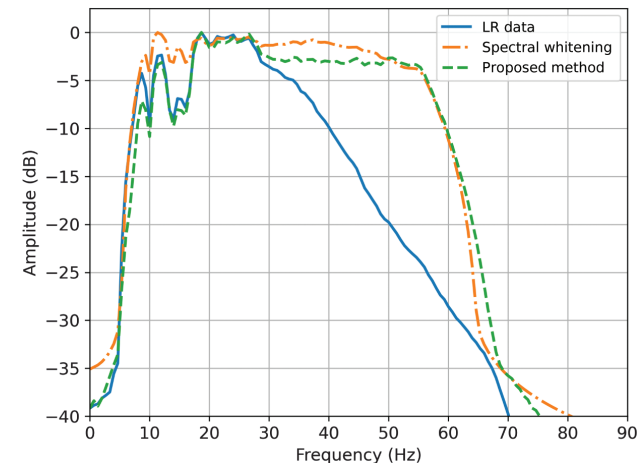


Figure 21. Comparison of normalized multitrace average amplitude spectra after resolution enhancement.

(Gao et al., 2024; Liu et al., 2024a) can be used to redistribute traces onto a pseudoregular grid. This process reduces acquisition footprints and enhances spatial continuity, which is critical for training the network to recognize coherent geologic patterns and suppress artifacts.

Cross-dip effects

Crossdip refers to geologic layers dipping perpendicular to the survey line. The irregular geometry of crooked-line surveys causes variations in dip orientation relative to the acquisition path, leading to mispositioned reflectors and spurious high-frequency components. To correct this, the 2.5D Kirchhoff migration (Jodeiri Akbari Fam et al., 2021) can be used. This migration technique accounts for azimuth-dependent velocity variations, aligning seismic events to their true subsurface positions. By preserving the geometries of reflectors, such as faults and stratigraphic boundaries, we believe this step provides reliable HR features for CycleGAN training.

Out-of-plane reflections

Out-of-plane reflections originate from structures outside the vertical plane of the 2D survey line. In crooked-line acquisition, the curved survey path can inadvertently capture such energy, introducing false structures (e.g., phantom reflectors). The 2.5D Kirchhoff migration can effectively suppress these artifacts by focusing seismic energy within the imaging plane. In addition, CycleGAN's cycle consistency loss (equation 4) helps eliminate inconsistencies during the resolution enhancement process, further reducing the impact of these artifacts.

A robust preprocessing workflow is essential to mitigate these challenges and ensure that CycleGAN learns geologically meaningful HR features. This process includes midpoint regularization, migration corrections, and artifact suppression. In addition, advanced preprocessing techniques with iterative velocity model updating can further refine the input data. Future research will explore optimizing acquisition parameters, such as increasing receiver density and using broader frequency sweeps, to enhance the effective bandwidth of 2D data. Broader frequency content would raise the resolution ceiling of our method, enabling the recovery of finer subsurface details, particularly in high-attenuation regions such as the Loess Plateau.

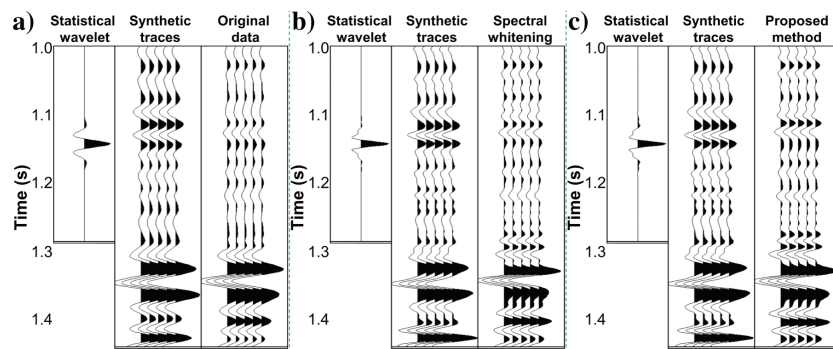


Figure 22. Well-log tie analysis. (a) Original LR data, (b) results by spectral whitening, and (c) results by the proposed method. Our proposed method provides better alignment with well-log data than spectral whitening.

CONCLUSION

The unique geologic structure of the Loess Plateau causes distinct seismic wave attenuation between 3D swath and 2D crooked-line acquisitions, generating data sets with varying resolutions. We develop a weakly supervised framework using bidirectional CycleGAN, integrating custom loss functions and data augmentation to enhance 3D data resolution guided by 2D HR crooked-line surveys. Ablation studies on synthetic data validate the critical roles of these components in achieving HR outcomes. In addition, synthetic data experiments demonstrate that our method outperforms traditional spectral whitening and spiking deconvolution, with quantitative metrics showing improved S/N and PCC. Qualitatively, our method achieves enhanced event continuity and preserves high-frequency details, mitigating the key limitations of conventional techniques. Field data results further confirm the efficacy of the proposed framework, showing satisfactory resolution improvements under challenging near-surface conditions. Unlike conventional methods, which struggle to recover natural high-frequency components attenuated by geologic effects such as loess layers, our framework leverages geophysically grounded high-frequency information from 2D HR references. This integration ensures the enhanced high-frequency features are realistic and physically meaningful, bridging the resolution gap between 2D and 3D data sets. These advancements enable more accurate geologic interpretations and support safer resource exploration. Future work will optimize the preprocessing of 2D crooked-line data, extend the framework to prestack seismic data, and incorporate more complex geologic structures. Furthermore, we aim to refine the network's adaptability to broader seismic exploration applications, potentially revolutionizing the seismic exploration practice with this innovative, weakly supervised framework.

ACKNOWLEDGMENTS

This work was supported in part by the National Key Research and Development Program of China under grant no. 2021YFA0716904, in part by the National Natural Science Foundation of China under grant no. 42374135, and in part by the Fundamental Research Funds for the Central Universities under grant no. xzy012023073. The contribution of the first author is supported by the industrial sponsors of the Signal Analysis and Imaging Group (SAIG) consortium at the University of Alberta.

DATA AND MATERIALS AVAILABILITY

Data associated with this research are available and can be obtained by contacting the corresponding author.

REFERENCES

- Baraniuk, R. G., 2007, Compressive sensing: IEEE Signal Processing Magazine, **24**, 118–121, doi: [10.1109/MSP.2007.4286571](https://doi.org/10.1109/MSP.2007.4286571).
- Bian, G., and L. Zhang, 1986, Spectral whitening of seismic data: Geophysical Prospecting for Petroleum, **2**, 26–33.
- Cai, A., H. Qiu, and F. Niu, 2022, Semi-supervised surface wave tomography with Wasserstein cycle-consistent GAN: Method and application to southern California plate boundary region: Journal

- of Geophysical Research: Solid Earth, **127**, e2021JB023598, doi: [10.1029/2021JB023598](https://doi.org/10.1029/2021JB023598).
- Chen, H., J. Gao, X. Jiang, Z. Gao, and W. Zhang, 2021, Optimization-inspired deep learning high-resolution inversion for seismic data: *Geophysics*, **86**, no. 3, R265–R276, doi: [10.1190/geo2020-0034.1](https://doi.org/10.1190/geo2020-0034.1).
- Cheraghi, S., M. Naghizadeh, D. Snyder, R. Haugaard, and T. Gemmell, 2020, High-resolution seismic imaging of crooked two-dimensional profiles in greenstone belts of the Canadian shield: Results from the Swayze Area, Ontario, Canada: *Geophysical Prospecting*, **68**, 62–81, doi: [10.1111/1365-2478.12854](https://doi.org/10.1111/1365-2478.12854).
- Chopra, S., and K. J. Marfurt, 2007, Volumetric curvature attributes add value to 3D seismic data interpretation: *The Leading Edge*, **26**, 856–867, doi: [10.1190/1.2756864](https://doi.org/10.1190/1.2756864).
- Duijndam, A., M. Schoneville, and C. Hindriks, 1999, Reconstruction of band-limited signals, irregularly sampled along one spatial direction: *Geophysics*, **64**, 524–538, doi: [10.1190/1.1444559](https://doi.org/10.1190/1.1444559).
- Gao, W., D. Liu, W. Chen, M. D. Sacchi, and X. Wang, 2024, NeRSI: Neural implicit representations for 5D seismic data interpolation: *Geophysics*, **90**, no. 1, V29–V42, doi: [10.1190/geo2023-0767.1](https://doi.org/10.1190/geo2023-0767.1).
- Goyes-Peñaflor, P., L. Suárez-Rodríguez, C. V. Correa, and H. Arguello, 2024, GAN-supervised seismic data reconstruction: An enhanced-learning for improved generalization: *IEEE Transactions on Geoscience and Remote Sensing*, **62**, 1–10, doi: [10.1109/TGRS.2024.3434474](https://doi.org/10.1109/TGRS.2024.3434474).
- Greer, S., and S. Fomel, 2018, Matching and merging high-resolution and legacy seismic images: *Geophysics*, **83**, no. 2, V115–V122, doi: [10.1190/geo2017-0238.1](https://doi.org/10.1190/geo2017-0238.1).
- He, K., X. Zhang, S. Ren, and J. Sun, 2016, Deep residual learning for image recognition: *Proceedings of the IEEE Conference on Computer Vision and Pattern Recognition*, 770–778.
- Isola, P., J.-Y. Zhu, T. Zhou, and A. A. Efros, 2017, Image-to-image translation with conditional adversarial networks: *Proceedings of the IEEE Conference on Computer Vision and Pattern Recognition*, 1125–1134.
- Jiang, Y., X. Gong, D. Liu, Y. Cheng, C. Fang, X. Shen, J. Yang, P. Zhou, and Z. Wang, 2021, EnlightenGAN: Deep light enhancement without paired supervision: *IEEE Transactions on Image Processing*, **30**, 2340–2349, doi: [10.1109/TIP.2021.3051462](https://doi.org/10.1109/TIP.2021.3051462).
- Jodeiri Akbari Fam, H., M. Naghizadeh, R. Smith, O. Yilmaz, S. Cheraghi, and K. Rubingh, 2023, High-resolution 2.5D multifocusing imaging of a crooked seismic profile in a crystalline rock environment: Results from the Larder Lake Area, Ontario, Canada: *Geophysical Prospecting*, **71**, 1152–1180, doi: [10.1111/1365-2478.13285](https://doi.org/10.1111/1365-2478.13285).
- Jodeiri Akbari Fam, H., M. Naghizadeh, and O. Yilmaz, 2021, 2.5D multi-focusing imaging of crooked-line seismic surveys: *Geophysics*, **86**, no. 6, S355–S369, doi: [10.1190/geo2020-0660.1](https://doi.org/10.1190/geo2020-0660.1).
- Kaur, H., N. Pham, and S. Fomel, 2020, Improving the resolution of migrated images by approximating the inverse Hessian using deep learning: *Geophysics*, **85**, no. 4, WA173–WA183, doi: [10.1190/geo2019-0315.1](https://doi.org/10.1190/geo2019-0315.1).
- Kazemeini, S. H., C. Yang, C. Juhlin, S. Fomel, and C. Cosma, 2010, Enhancing seismic data resolution using the prestack blueing technique: An example from the Ketzin CO₂ injection site, Germany: *Geophysics*, **75**, no. 6, V101–V110, doi: [10.1190/1.3483900](https://doi.org/10.1190/1.3483900).
- Ke, X., Y. Shi, X. Fu, L. Song, H. Jing, J. Yang, and Z. Zhang, 2023, The Nth power Fourier spectrum analysis for the generalized seismic wavelets: *IEEE Transactions on Geoscience and Remote Sensing*, **61**, 1–10, doi: [10.1109/TGRS.2023.3243184](https://doi.org/10.1109/TGRS.2023.3243184).
- Keiner, J., S. Kunis, and D. Potts, 2009, Using NFFT 3 – A software library for various nonequispaced fast Fourier transforms: *ACM Transactions on Mathematical Software*, **36**, 1–30, doi: [10.1145/1555386.1555388](https://doi.org/10.1145/1555386.1555388).
- Kim, J., S. J. Lee, Y. S. Seo, and H. T. Ju, 2014, Enhancement of seismic stacking energy with crossdip correction for crooked survey lines: *The Journal of Engineering Geology*, **24**, 171–178, doi: [10.9720/kseg.2014.2.171](https://doi.org/10.9720/kseg.2014.2.171).
- Kingma, D. P., and J. Ba, 2014, Adam: A method for stochastic optimization: arXiv preprint, doi: [10.48550/arXiv.1412.6980](https://doi.org/10.48550/arXiv.1412.6980).
- Lancaster, S., and D. Whitcombe, 2000, Fast-track ‘coloured’ inversion: 70th Annual International Meeting, SEG, Expanded Abstracts, 1572–1575, doi: [10.1190/1.1815711](https://doi.org/10.1190/1.1815711).
- Leinbach, J., 1995, Wiener spiking deconvolution and minimum-phase wavelets: A tutorial: *The Leading Edge*, **14**, 189–192, doi: [10.1190/1.1437110](https://doi.org/10.1190/1.1437110).
- Li, J., X. Wu, and Z. Hu, 2021, Deep learning for simultaneous seismic image super-resolution and denoising: *IEEE Transactions on Geoscience and Remote Sensing*, **60**, 1–11, doi: [10.1109/TGRS.2021.3057857](https://doi.org/10.1109/TGRS.2021.3057857).
- Li, Y., G. Zhang, J. Duan, C. He, H. Du, F. Luo, Y. Zhan, and J. Wang, 2020, Extended stable factor method for the inverse Q-filter: *Geophysics*, **85**, no. 3, T155–T163, doi: [10.1190/geo2019-0502.1](https://doi.org/10.1190/geo2019-0502.1).
- Lin, L., Z. Zhong, C. Cai, C. Li, and H. Zhang, 2024, SeisGAN: Improving seismic image resolution and reducing random noise using a generative adversarial network: *Mathematical Geosciences*, **56**, 723–749, doi: [10.1007/s11004-023-10103-8](https://doi.org/10.1007/s11004-023-10103-8).
- Liu, D., W. Gao, W. Xu, J. Li, X. Wang, and W. Chen, 2024a, 5-D seismic data interpolation by continuous representation: *IEEE Transactions on Geoscience and Remote Sensing*, **62**, 1–11, doi: [10.1109/TGRS.2024.3431439](https://doi.org/10.1109/TGRS.2024.3431439).
- Liu, D., Y. He, X. Wang, M. D. Sacchi, W. Chen, G. Du, and M. Zhang, 2025, From shallow to deep: Enhancing seismic resolution with weak supervision: *Geophysics*, **90**, no. 3, doi: [10.1190/geo2024-0502.1](https://doi.org/10.1190/geo2024-0502.1).
- Liu, D., W. Niu, X. Wang, M. D. Sacchi, W. Chen, and C. Wang, 2023, Improving vertical resolution of vintage seismic data by a weakly supervised method based on cycle generative adversarial network: *Geophysics*, **88**, no. 6, V445–V458, doi: [10.1190/geo2023-0006.1](https://doi.org/10.1190/geo2023-0006.1).
- Liu, D., M. Zhou, X. Wang, Z. Shi, M. D. Sacchi, W. Chen, Z. Liu, and X. Wang, 2024b, Enhancing ground penetrating radar (GPR) data resolution through weakly supervised learning: *IEEE Transactions on Geoscience and Remote Sensing*, **62**, 1–13, doi: [10.1109/TGRS.2024.3410184](https://doi.org/10.1109/TGRS.2024.3410184).
- Malehmir, A., and G. Bellefleur, 2016, Pros and cons of 2D crooked seismic profiles for deep mineral exploration — A comparison with 3D surveys in geologically complex mining environment: EAGE/DGG Workshop on Deep Mineral Exploration, doi: [10.3997/2214-4609.201600031](https://doi.org/10.3997/2214-4609.201600031).
- Merrifield, T. P., D. P. Griffith, S. A. Zamanian, S. Gesbert, S. Sen, J. De La Torre Guzman, R. D. Potter, and H. Kuehl, 2022, Synthetic seismic data for training deep learning networks: *Interpretation*, **10**, no. 3, SE31–SE39, doi: [10.1190/INT-2021-0193.1](https://doi.org/10.1190/INT-2021-0193.1).
- Naghadeh, D. H., and C. K. Morley, 2017, Enhancement of temporal resolution using improved time-variant spectral whitening: *Journal of Geophysics and Engineering*, **14**, 822–832, doi: [10.1088/1742-2140/a6ddf](https://doi.org/10.1088/1742-2140/a6ddf).
- Nedimović, M. R., S. Mazzotti, and R. D. Hyndman, 2003, Three-dimensional structure from feathered two-dimensional marine seismic reflection data: The eastern Nankai Trough: *Journal of Geophysical Research: Solid Earth*, **108**, 1–14, doi: [10.1029/2002JB001959](https://doi.org/10.1029/2002JB001959).
- Nedimović, M. R., and G. F. West, 2003, Crooked-line 2D seismic reflection imaging in crystalline terrains: Part 1, data processing: *Geophysics*, **68**, 274–285, doi: [10.1190/1.1543213](https://doi.org/10.1190/1.1543213).
- Robinson, E. A., and S. Treitel, 2000, Geophysical signal analysis: SEG.
- Saatçilar, R., S. İnan, A. Cankurtaranlar, F. Duygun, E. Demirbag, S. Ergintav, M. Yılmaz, A. R. Toygar, A. Kösebalaban, and M. N. Yalçın, 2014, An environmentally-friendly integrated seismic imaging for coal exploration in the Miocene Soma Basin, Western Turkey: *International Journal of Oil, Gas and Coal Technology*, **7**, 399–414, doi: [10.1504/IJOGCT.2014.062171](https://doi.org/10.1504/IJOGCT.2014.062171).
- Sacchi, M. D., 1997, Reweighting strategies in seismic deconvolution: *Geophysical Journal International*, **129**, 651–656, doi: [10.1111/j.1365-246X.1997.tb04500.x](https://doi.org/10.1111/j.1365-246X.1997.tb04500.x).
- Schmelzbach, C., C. Juhlin, R. Carbonell, and J. F. Simanca, 2007, Prestack and poststack migration of crooked-line seismic reflection data: A case study from the South Portuguese Zone fold belt, southwestern Iberia: *Geophysics*, **72**, no. 2, B9–B18, doi: [10.1190/1.2407267](https://doi.org/10.1190/1.2407267).
- Sui, Y., and J. Ma, 2020, Blind sparse-spike deconvolution with thin layers and structure: *Geophysics*, **85**, no. 6, V481–V496, doi: [10.1190/geo2019-0423.1](https://doi.org/10.1190/geo2019-0423.1).
- Sun, S., G. Li, R. Ding, L. Zhao, Y. Zhang, S. Zhao, J. Zhang, and J. Ye, 2023, Seismic random noise suppression using improved cyclegan: *Frontiers in Earth Science*, **11**, 1102656, doi: [10.3389-feart.2023.1102656](https://doi.org/10.3389-feart.2023.1102656).
- Taylor, H. L., S. C. Banks, and J. F. McCoy, 1979, Deconvolution with the L₁ norm: *Geophysics*, **44**, 39–52, doi: [10.1190/1.1440921](https://doi.org/10.1190/1.1440921).
- Tian, A.-W., Z.-S. Li, S.-T. Liu, Z.-S. Wang, G.-H. Zheng, Z.-H. Yuan, and H. Huang, 2021, Research on seismic exploration techniques and methods in urban environment of Loess Plateau: IOP Conference Series: Earth and Environmental Science, **660**, 012003, doi: [10.1088/1755-1315/660/1/012003](https://doi.org/10.1088/1755-1315/660/1/012003).
- Wadas, S. H., U. Polom, and C. M. Krawczyk, 2016, High-resolution shear-wave seismic reflection as a tool to image near-surface subrosion structures — A case study in Bad Frankenhausen, Germany: *Solid Earth Sciences Library*, **7**, 1491–1508, doi: [10.5194/se-2016-91](https://doi.org/10.5194/se-2016-91).
- Wang, X., W. Chen, and Z. Zhu, 2018, Robust seismic volumetric dip estimation combining structure tensor and multiwindow technology: *IEEE Transactions on Geoscience and Remote Sensing*, **57**, 395–405, doi: [10.1109/TGRS.2018.2854777](https://doi.org/10.1109/TGRS.2018.2854777).
- Wang, X., L. Zhang, Q. Liang, C. Jiang, W. Wang, Y. Xiaolong, H. Shi, C. Zhao, C. Hinz, Q. Liu, P. Van Barren, M. Zhang, X. Zou, and B. Liang, 2014, Full-azimuth, high-density, 3D point-source/point-receiver seismic survey for shale gas exploration in a Loess Plateau: A case study from the Ordos Basin, China: *First Break*, **32**, 105–112, doi: [10.3997/1365-2397.32.9.7790](https://doi.org/10.3997/1365-2397.32.9.7790).
- Wang, Y., 2006, Inverse Q-filter for seismic resolution enhancement: *Geophysics*, **71**, no. 3, V51–V60, doi: [10.1190/1.2192912](https://doi.org/10.1190/1.2192912).
- Wang, Y., X. Hu, J. M. Harris, and H. Zhou, 2022a, Crosswell seismic imaging using Q-compensated viscoelastic reverse time migration with explicit stabilization: *IEEE Transactions on Geoscience and Remote Sensing*, **60**, 1–11, doi: [10.1109/TGRS.2022.3176749](https://doi.org/10.1109/TGRS.2022.3176749).
- Wang, Y.-Q., Q. Wang, W.-K. Lu, Q. Ge, and X.-F. Yan, 2022b, Seismic impedance inversion based on cycle-consistent generative adversarial network: *Petroleum Science*, **19**, 147–161, doi: [10.1016/j.petisci.2021.09.038](https://doi.org/10.1016/j.petisci.2021.09.038).
- Wang, Z., J. Chen, and S. C. Hoi, 2020, Deep learning for image super-resolution: A survey: *IEEE transactions on Pattern Analysis and Machine Intelligence*, **43**, 3365–3387, doi: [10.1109/TPAMI.2020.2982166](https://doi.org/10.1109/TPAMI.2020.2982166).

- Wei, Y., Z. Zhang, Y. Wang, M. Xu, Y. Yang, S. Yan, and M. Wang, 2021, DerainCycleGAN: Rain attentive CycleGAN for single image deraining and rainmaking: *IEEE Transactions on Image Processing*, **30**, 4788–4801, doi: [10.1109/TIP.2021.3074804](https://doi.org/10.1109/TIP.2021.3074804).
- Wiggins, R. A., 1978, Minimum entropy deconvolution: *Geoexploration*, **16**, 21–35, doi: [10.1016/0016-7142\(78\)90005-4](https://doi.org/10.1016/0016-7142(78)90005-4).
- Wu, J., 1996, Potential pitfalls of crooked-line seismic reflection surveys: *Geophysics*, **61**, 277–281, doi: [10.1190/1.1443949](https://doi.org/10.1190/1.1443949).
- Xia, J., and Y. Dai, 2024, A deep ground roll noise suppression method based on DRinCGAN: *IEEE 2nd International Conference on Control, Electronics and Computer Technology*, 1259–1264.
- Xu, W., H. Liu, H. Mi, B. Zhang, J. Guo, Y. Ge, and J. You, 2024, High-precision Q modeling and Q migration technology and its applications in Loess Plateau regions: *Applied Geophysics*, **21**, 835–847, doi: [10.1007/s11770-024-1110-y](https://doi.org/10.1007/s11770-024-1110-y).
- Xue, Y.-J., J.-X. Cao, and X.-J. Wang, 2019, Inverse Q filtering via synchrosqueezed Wavelet transform: *Geophysics*, **84**, no. 2, V121–V132, doi: [10.1190/geo2018-0177.1](https://doi.org/10.1190/geo2018-0177.1).
- Yang, B., K. Gong, H. Liu, Q. Li, and W. Zhu, 2024, Anatomically guided PET image reconstruction using conditional weakly-supervised multi-task learning integrating self-attention: *IEEE Transactions on Medical Imaging*, **43**, 2098–2112, doi: [10.1109/TMI.2024.3356189](https://doi.org/10.1109/TMI.2024.3356189).
- Yao, Z., J. Chen, W. Ren, H. Qian, and M. Li, 2004, Seismic data acquisition techniques on loess hills in the Ordos Basin: *Applied Geophysics*, **1**, 115–121, doi: [10.1007/s11770-004-0013-1](https://doi.org/10.1007/s11770-004-0013-1).
- Ye, H., 2011, Seismic acquisition parameters on Loess Plateau: *Procedia Earth and Planetary Science*, **3**, 370–374, doi: [10.1016/j.proeps.2011.09.108](https://doi.org/10.1016/j.proeps.2011.09.108).
- Yuan, Y., S. Liu, J. Zhang, Y. Zhang, C. Dong, and L. Lin, 2018, Unsupervised image super-resolution using cycle-in-cycle generative adversarial networks: *IEEE/CVF Conference on Computer Vision and Pattern Recognition Workshops*, 814–819.
- Yurui, L., Z. Xuanchang, C. Zhi, L. Zhengjia, L. Zhi, and L. Yansui, 2021, Towards the progress of ecological restoration and economic development in China's Loess Plateau and strategy for more sustainable development: *Science of the Total Environment*, **756**, 143676, doi: [10.1016/j.scitotenv.2020.143676](https://doi.org/10.1016/j.scitotenv.2020.143676).
- Zhang, H., W. Wang, X. Wang, W. Chen, Y. Zhou, C. Wang, and Z. Zhao, 2019, An implementation of the seismic resolution enhancing network based on GAN: 89th Annual International Meeting, SEG, Expanded Abstracts, 2478–2482, doi: [10.1190/segam2019-3216229.1](https://doi.org/10.1190/segam2019-3216229.1).
- Zhang, H.-R., Y. Liu, Y.-H. Sun, and G. Chen, 2024a, SeisResoDiff: Seismic resolution enhancement based on a diffusion model: *Petroleum Science*, **21**, 3166–3188, doi: [10.1016/j.petsci.2024.07.002](https://doi.org/10.1016/j.petsci.2024.07.002).
- Zhang, J., J. Wu, and X. Li, 2013, Compensation for absorption and dispersion in prestack migration: An effective Q approach: *Geophysics*, **78**, no. 1, S1–S14, doi: [10.1190/geo2012-0128.1](https://doi.org/10.1190/geo2012-0128.1).
- Zhang, W., J. Gao, Y. Shi, X. Ke, Z. Li, T. Yang, and W. Sun, 2024b, Q-compensated image-domain least-squares reverse time migration through preconditioned point-spread functions: *Geophysics*, **89**, no. 3, S195–S213, doi: [10.1190/geo2023-0333.1](https://doi.org/10.1190/geo2023-0333.1).
- Zhang, W., M. Ravasi, J. Gao, and Y. Shi, 2024c, Deep-unrolling architecture for image-domain least-squares migration: *Geophysics*, **89**, no. 3, S215–S234, doi: [10.1190/geo2023-0428.1](https://doi.org/10.1190/geo2023-0428.1).
- Zhang, Y., H. Zhou, Y. Wang, M. Zhang, B. Feng, and W. Wu, 2022, A novel multichannel seismic deconvolution method via structure-oriented regularization: *IEEE Transactions on Geoscience and Remote Sensing*, **60**, 1–10, doi: [10.1109/TGRS.2022.3141113](https://doi.org/10.1109/TGRS.2022.3141113).
- Zhao, H., O. Gallo, I. Frosio, and J. Kautz, 2016, Loss functions for image restoration with neural networks: *IEEE Transactions on Computational Imaging*, **3**, 47–57, doi: [10.1109/TCI.2016.2644865](https://doi.org/10.1109/TCI.2016.2644865).
- Zhao, X., Y. Gao, S. Guo, W. Gu, and G. Li, 2023, Seismic resolution enhancement using a cycle generative adversarial neural network with pseudo-well data: *Applied Sciences*, **13**, 12980, doi: [10.3390/app132412980](https://doi.org/10.3390/app132412980).
- Zhu, J., T. Park, P. Isola, and A. A. Efros, 2017, Unpaired image-to-image translation using cycle-consistent adversarial networks: *Proceedings of the IEEE International Conference on Computer Vision*, 2223–2232.

Biographies and photographs of the authors are not available.